MASTERARBEIT

Correlation effects in high harmonic generation

zur Erlangung des akademischen Grades
Diplom-Ingenieur/in

im Rahmen des Studiums
Technische Physik

unter der Anleitung von
Ass. Prof. Dr. Iva Březinová
Institut für Theoretische Physik

eingereicht von

Katharina Buczolich
11779641

Contents

1. Introduction

In the process of high harmonics generation (HHG) a high intensity low frequency field interacting with (typically) an atomic gas target generates higher orders of its frequency [1], [2]. HHG has opened the doors to attosecond physics. Nowadays it is possible to create fields containing 50000 times the driving frequency [3]. The resulting spectrally broad pulses allow for generation of trains of ultrashort pulses. These pulses can get as short as a few attoseconds in time, the natural timescale of electrons, allowing the observation of fundamental processes such as the formation of chemical bonds [4] or the photoelectrical effect [5], [6] on their natural time scale. Furthermore, the process enabled the development of tabletop sized short wavelength sources [3], [7]. Attosecond physics is an active field of research and this year (2023) even the Nobel price was awarded towards it. It was awarded to Anne L'Huillier for the generation of high harmonics themselves and her work towards generating attosecond pulses, together with Pierre Agostini and Ferenc Krausz for making measurements at this time scale possible [8], [9], [10].

For this breakthroughs a close exchange between experimental and theoretical developments was important. From first calculations mostly driven by Kenneth Kulander [11], [12] using the time-dependent single-active electron approximation, over Paul Corkum's intuitive description for HHG [13] to Maciej Lewenstein's work [14], HHG was for a long time widely described as a single-electron effect. Even though this approximation is able to give a qualitatively correct understanding of HHG, multi-electron dynamics are important for an accurate description of atoms and ions with more than one electron. The strong-field regime of HHG is challenging for numerical work and only a limited number of methods are able to describe it. For smaller systems correlated electron calculations are either performed using the multi-configurational time-dependent Hartree-Fock method (MCTDHF) [15], [16] or the R-matrix method [17]. For larger systems the time-dependent configuration interaction singles (TDCIS)[18] method is usually used.

To circumvent the challenges associated with a multi-electron wavefunction ansatz the time-dependent two-particle reduced-density (TD2RDM) method [19] has been developed. It has been shown to be applicable to HHG in atoms like beryllium and neon [19]. In the present thesis, we will apply the TD2RDM method to larger atoms and benchmark its accuracy towards exact results. For this purpose we will employ the separation of spaces for electrons as done in the time-dependent complete active-space self-consistent field (TDCASSCF) [20] method. Furthermore we apply measures of correlation from quantum information theory [21] and observe their time-dependence during the process of HHG. With this we want to quantitatively assess the importance of correlations during

HHG.
This thesis is structured as followed: In the second chapter, we review the models used to describe HHG. In the third chapter, we will give an overview of numerical methods, widely used to simulate HHG in atoms. Thereby, special emphasis is given on MCTDHF, TDCASSCF and the TD2RDM method. In chapter four, measures of correlation and entanglement with special emphasis on fermionic systems will be discussed. In chapter five, we will discuss an interface procedure, which allows us to use the MCTDHF ground state as an input for the TD2RDM calculations. Finally in chapter six, we will present calculations of HHG and analyse the time dependency of different correlations measures during this process. There different parameter regimes, such as different atoms, i.e. beryllium, neon, and argon, and different laser parameters are investigated. In this work we use atomic units with $\hbar = m = e = 1$ where m and $-e$ are the electron mass and charge, respectively.

2. High harmonic generation

High harmonic generation (HHG) is the fundamental process, which gave rise to attosecond physics. It was first discovered in the late 1980's [1], [2] when laser technology was advanced enough to produce the necessary strong driving fields. Typically the targets are gases of noble gas atoms, which then emit odd multiples of the driving frequency. A qualitative sketch of the spectrum can be seen in Figure 2.1.

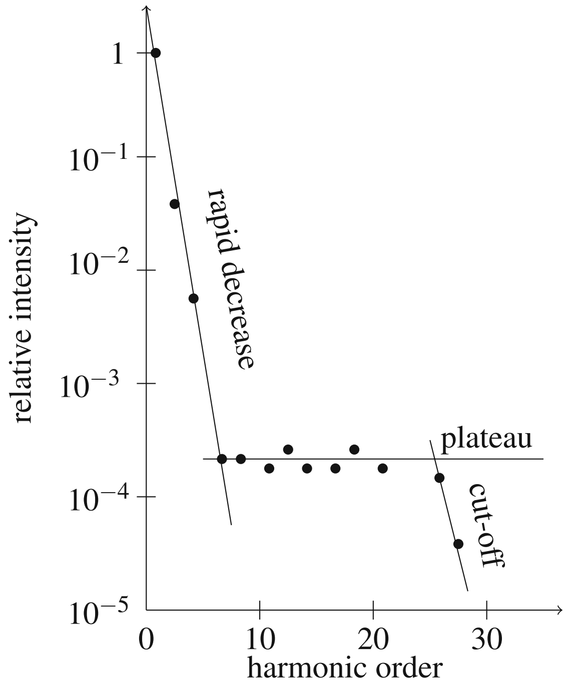

Figure 2.1.: Qualitative HHG spectrum.

The harmonics initially decay exponentially with the order as expected from perturbation theory, followed by an extended plateau of almost constant intensity and then an abrupt cut-off. A first simple semi-classical approach to describe the phenomenon was given by Corkum [13], which captures the essential physics and is able to described the cut-off quite accurately. This model will be explained in section 2.2. Then Lewenstein [14] introduced a quantum description of the effect, employing the single-electron approximation, which, while being in good agreement with the semi-classical approach, gives more insight into the process. The most important steps in Lewenstein's approach will be shortly summarised in section 2.3.

2.1. Strong field physics

In the present thesis, our calculations will be restricted to the spectrum emitted by a single atom, while bearing in mind that a full description requires to take into account propagation effects in the gas medium [22]. One fundamental process in HHG, i.e. the ionisation step, can be analysed by means of the Keldysh parameter [23]

$$\gamma = \sqrt{\frac{I_p}{2U_p}}, \tag{2.1}$$

which distinguishes between the regime of tunnel ionisation when $\gamma \ll 1$, and multi-photon ionisation when $\gamma \gg 1$. I_p is the ionisation potential of the atom and $U_p = \frac{F_0^2}{4\omega^2}$ is the pondermotive energy of the electron in the laser field, where F_0 is the amplitude of the electric field and ω is the frequency of the laser field. The Keldysh parameter can be viewed as the ratio between the tunnelling time and the time it takes for the laser field to bend the potential back to its field free position [24].

2.2. Three step model

The semi-classical model [13], which is often also called the three-step model, explains HHG in three steps. A schematic overview of the process is given in Figure 2.2.

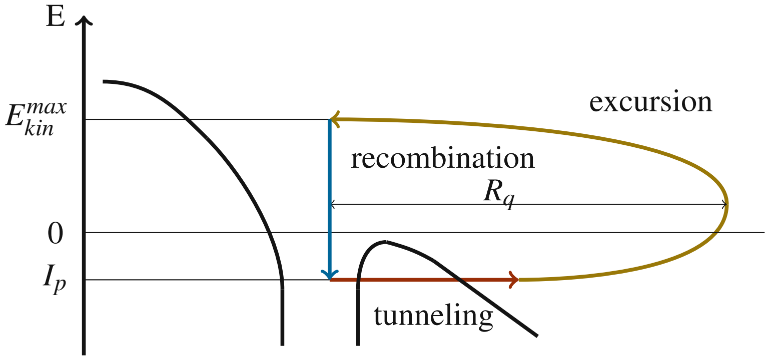

Figure 2.2.: Schematic picture of the three-step model.

First, the electron tunnels through the barrier created by the nuclear potential and the strong laser field. After tunneling, the electron is approximated to have zero velocity and its motion in the laser field is described neglecting the nuclear potential. The probability of this process can be described via the ionisation probability N_{ion}, which can be approximated by the ADK model for ionisation [25]. The free electron is then accelerated by the laser field, gaining kinetic energy. The amount of energy upon recombination depends on the ionisation time t_{ion} and its maximum is given by $E_{max}^{kin} = 3.17U_p$. The excursion radius for this three-step model is called the quiver radius $R_q = \frac{F_0}{\omega^2}$. If the electron returns to the ion at time t_{rec}, it recombines with a probability of P_{rec} and emits its kinetic energy plus the ionisation energy as radiation. This gives already an accurate estimate of the maximal possible emitted energy, i.e. the cut-off energy, as

$$E_{max} \approx 3.17U_p + I_p. \tag{2.2}$$

As an example (see also section 6.3 below) an argon atom with the ionisation energy of 15.6 eV [26] driven in a 780 nm laser field with $I = 3.5 \times 10^{14}\ \mathrm{W\,cm^{-2}}$, gives rise to a cut-off at 78 eV with the ponderomotive energy of 19.71 eV. As the time t_{ion} at which the electron gets ionised is not fixed, all lower energies do appear in the spectrum too. Furthermore, this simple model is already able to describe the appearance of only odd harmonics. Because of the point symmetry of the problem, all even contributions cancel out.

2.3. Lewenstein model

A more accurate quantum description for HHG was later introduced by Lewenstein et al. [14]. The model is similar to the three-step model but accounts for quantum probabilities, e.g. for the tunnel ionisation. The dipole moment of the atom for a given time t can be written as

$$z(t) = i\int_0^t dt' \int d^3\vec{p}\; F_0\cos(t')\,d_z(\vec{p}-\vec{A}(t'))\,d_z^*(\vec{p}-\vec{A}(t))\,e^{-iS(\vec{p},t,t')} + c.c., \tag{2.3}$$

where $d_z = \langle e|z|g\rangle$ is the atomic dipole matrix element for transitions from the ground state $|g\rangle$ to unbound states $|e\rangle$, and

$$S(\vec{p},t,t') = \int_{t'}^{t} dt'' \left(\frac{[\vec{p}-\vec{A}(t'')]^2}{2} + I_p \right), \tag{2.4}$$

is the action. $F_0\cos(t')d_z(\vec{p}-\vec{A}(t'))$ is the ionisation probability amplitude in the laser field and $d_z^*(\vec{p}-\vec{A}(t))$ is the recombination probability amplitude. $\vec{p}$ is the canonical momentum and $\vec{A}$ is the vector potential. $e^{-iS(\vec{p},t,t')}$ is the phase gained by propagation in the field. The electrical field is assumed to be linearly polarised in z-direction. With the dipole moment $z(t)$ or the dipole acceleration $a_z(t) = \ddot{z}(t)$ we can evaluate the high harmonic spectrum using the classical Lamor formula [27]:

$$I_z(\omega) = \frac{2\omega^4}{3c^3}\left|\frac{1}{t_f - t_i}\int_{t_i}^{t_f} z(t)e^{-i\omega t}\right|^2, \tag{2.5}$$

$$I_a(\omega) = \frac{2}{3c^3}\left|\frac{1}{t_f - t_i}\int_{t_i}^{t_f} a_z(t)e^{-i\omega t}\right|^2. \tag{2.6}$$

By comparison to Equation 2.3, we can give an estimate of the intensity of the spectra, i.e. the harmonic yield as

$$I(t_{rec}) \approx \dot{N}_{ion}(t_{ion})\, P_{rec}(t_{rec}), \tag{2.7}$$

which is given by the ionisation rate $\dot{N}_{ion}(t_{ion})$ of the electron at the time t_{ion} times the recombination probability $P_{rec}(t_{rec})$ at t_{rec}. The Lewenstein model predicts for the cut-off energy the well-known formula of

$$E_{max} \approx 3.17U_p + 1.3I_p, \tag{2.8}$$

where the factor of 1.3 holds for $I_p \ll U_p$.

3. Methods for solving the multi-electron atom Hamiltonian

Direct solution of the multi-electron Schrödinger equation with all its electron-electron interactions is not possible for more than two electrons [28], [29]. Finding accurate approximative models and solving them is an active, numerically intensive, field of theoretical physics. In the following, we will discuss some state-of-the-art approximations for multi-electron atoms and review the necessary formulas for the numerical results presented later in this work. We will give an overview over wavefunction based methods here, which are later used as benchmarks for TD2RDM, which will be reviewed in section 3.4.

3.1. The Hamiltonian for multi-electron atoms

The full field-free Hamiltonian for an N-electron atom is given by

$$H = \sum_{i=1}^{N} \left[-\frac{1}{2}\nabla_i^2 - \frac{Z}{r_i} + \frac{1}{2}\sum_{j\neq i} U(\mathbf{r}_i, \mathbf{r}_j) \right], \tag{3.1}$$

where Z is the nuclear charge, and r_i is the the radial component of the i-th electron with respect to the origin at the nucleus. U describes the electron-electron interaction as

$$U(\mathbf{r}_1, \mathbf{r}_2) = \frac{1}{r_{12}} = \frac{1}{|\mathbf{r}_1 - \mathbf{r}_2|}. \tag{3.2}$$

By minimal coupling, we can substitute the canonical momentum as $\mathbf{p} = -i\nabla \rightarrow \mathbf{p} = -i\nabla + \frac{1}{c}\mathbf{A}(\mathbf{r}, t)$ to introduce coupling to an external field with the vector potential $\mathbf{A}$. If the wavelength of the field is large compared to the system, the dipole approximation, $\mathbf{A}(\mathbf{r}, t) = \mathbf{A}(\mathbf{t})$, can be used. The square of the vector potential is then independent of the position and can be transformed away from the Hamiltonian. With this the field-dependent Hamiltonian can be written as

$$H(t) = \sum_{i=1}^{N} \left[-\frac{1}{2}\nabla_i^2 - \frac{Z}{r_i} + \frac{1}{2c}\mathbf{A}(t)\nabla_i + \frac{1}{2}\sum_{j\neq i} U(\mathbf{r}_i, \mathbf{r}_j) \right]. \tag{3.3}$$

The field term, which is also the only explicitly time-dependent term, is then often denoted as $V_{ext}(t)$. By gauge transformation from the so-called velocity gauge Equation 3.3 to the length gauge, the external potential can be written as $V_{ext} = \mathbf{F}(t)\mathbf{r}$. This gauge is also widely used in strong-field physics.

3.2. Single-active electron approximation

Historically, a full numerical solution of the time-dependent Schrödinger equation in strong-field driving became possible in the 90s [27], however, with the restriction to the dynamics of only one electron. Therefore, the overview of numerical methods will start with the so-called single-active electron approximation.
The assumption that only one electron significantly contributes to the generation of HHG is valid as long as the field does not induce non-negligible two-electron ionisation. One can then approximate the multi-electron target atom with model potentials as is done within the single-active electron (SAE) approximation. The Schrödinger equation for that one electron can be written as

$$i\partial_t \left|\psi(t)\right\rangle = \left[H_{SAE} + V_{ext}(t)\right] \left|\psi(t)\right\rangle, \tag{3.4}$$

where $H_{SAE} = -\frac{1}{2}\nabla^2 + V_{PS}(\mathbf{r})$ includes the kinetic energy operator and a pseudo-potential $V_{PS}(\mathbf{r})$, that imitates all the other electrons. The solution for $\psi(t)$ can then be found by exponentiation

$$\left|\psi(t)\right\rangle = Te^{i\int(H_{SAE}+V_{ext}(t))dt} \left|\psi(0)\right\rangle, \tag{3.5}$$

where T is the time-ordering operator, which is usually performed by a split-step method. The SAE approximation is not able to describe any time-dependence of the (N-1) remaining electrons.

3.3. Methods based on the multi-electron wavefunction

In order to include more than one electron, a natural ansatz is to find a multi-electron wavefunction that satisfies Equation 3.3.

3.3.1. Time-dependent Hartree-Fock

Within the time-dependent Hartree-Fock (TDHF) method, the total many-body wavefunction is restricted to one single Slater determinant

$$\left|I(t)\right\rangle = \left|\phi_{1\uparrow}(t)\phi_{1\downarrow}(t)\ldots\phi_{N/2\uparrow}(t)\phi_{N/2\downarrow}(t)\right\rangle, \tag{3.6}$$

with orbitals $\{\phi_i(t)\}_{i=1}^{N/2}$, that are each occupied by one spin-up ↑ and one spin-down ↓ electron. The equations of motions for the orbitals can be found by employing the Dirac-Frenkel variational principle. This gives

$$i\partial_t \left|\phi_i\right\rangle = \big(-\frac{1}{2}\nabla^2 - \frac{Z}{r} + V_{ext}(t)\big)\left|\phi_i\right\rangle + \sum_{j=1}^{N/2}\big(2\left\langle\phi_j\right| U \left|\phi_j\right\rangle\left|\phi_i\right\rangle - \left\langle\phi_j\right| U \left|\phi_i\right\rangle\left|\phi_j\right\rangle\big). \quad (3.7)$$

The first term in the interaction contribution is called the Hartree-term and treats the interaction of one electron by the charge density of all the other electrons. The second term is called the Fock-term, and describes the exchange interaction between the electrons. This approximation is also known as the mean-field approximation. Since the system is described by a single Slater determinant, each orbital is always occupied by two electrons. Therefore, TDHF is not able to correctly distinguish between single and double ionisation.

3.3.2. Time-dependent configuration interaction

Within time-dependent configuration interaction (TDCI) the wave function is constructed from many Slater determinants, which are built from time-independent orbitals. The total wave function is then given as a linear combination of these Slater determinants as

$$\left|\Psi(t)\right\rangle = \sum_I C_I(t)\left|I\right\rangle, \quad (3.8)$$

where the $C_I(t)$ are called configuration interaction (CI) coefficient. The dynamics is solely described by the CI coefficients. Since the orbital basis is not adjustable, choosing an inappropriate basis might lead to a large number of orbitals required for converged results. For an equal number $N/2$ of spin-up and spin-down electrons the number of possible configurations Π for J orbitals is given by

$$\Pi = \binom{J}{N/2}^2, \quad (3.9)$$

and grows exponentially or even factorial depending on J and the number of electrons N. Consequently, especially for strong field applications, this method is often numerically unfeasible. To bybass the exponential growth, the CI-coefficients are often restricted to only allow for single- (TDCIS) or single- and double-excitations (TDCISD) by neglecting the Slater determinants which would correspond to higher excitations [30]. These methods are able to more accurately describe ionisation, however, approximations are made for the treatment of the electron-electron correlations.

Multi-configurational time-dependent Hartree-Fock (MCTDHF), on the other hand, tries to partially circumvent the problem of large (and growing) orbital basis sets by using time-dependent orbitals

$$|\Psi(t)\rangle = \sum_I C_I(t)\,|I(t)\rangle\,. \tag{3.10}$$

Even in strong-field applications, this choice drastically reduces the number of orbitals needed to about $J \approx N$ [31]. Such full-CI methods include the complete electron-electron correlation and are therefore considered the most accurate.

3.3.3. Time-dependent complete-active-space self-consistend-field

The time-dependent complete-active-space self-consistend-field (TDCASSCF) method developed by Sato et al. [20] is especially well suited for larger atoms. Here the orbitals are further separated into frozen core orbitals, dynamical core orbitals, and active orbitals. While frozen core orbitals have no time dependence, dynamical core orbitals are time dependent, and for both types of core orbitals the occupation is fixed as fully occupied. Active orbitals, on the other hand, are time-dependent and have time varying occupation numbers, as in the MCTDHF method. Figure 3.1 shows a schematic picture of this separation. Here, all active electrons are depicted in the lowest possible orbitals, but they can also occupy all other active orbitals resulting in partial occupation numbers for all active orbitals.

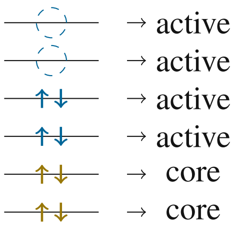

Figure 3.1.: Separation into active and core space.

This separation allows an efficient description of larger atoms, where the inner orbitals usually do not contribute to most physical phenomena, which we would like to investigate because of their strong binding. The resulting total wave function is given by

$$|\Psi_{CAS}\rangle = A\left[\left|\Phi_{fc}\right\rangle |\Phi_{dc}(t)\rangle \sum_I C_I(t)\,|\Phi_I(t)\rangle\right], \tag{3.11}$$

where $|\Phi_I(t)\rangle$ is a Slater determinant build from active orbitals $\{\phi_i(t)\}$, $\left|\Phi_{fc}\right\rangle$ and $|\Phi_{dc}(t)\rangle$ are Slater determinants built from frozen core and dynamical core orbitals, respectively, and A is the antisymmetrization operator. In this thesis, MCTDHF is used for smaller atoms, such as beryllium and neon, while TDCASSCF is used for larger atoms, such as argon and xenon. In the following, the equations of motion and some technical details of this method are presented.

Equations of motion and gauge freedom

The Dirac-Frenkel variational principle leads to the equations of motion (EOMs) for the orbitals ϕ, which build-up the Slater determinants, and the CI coefficients (for more details see [15]). However, the Dirac-Frenkel variational method does not fully determine the EOMs for the orbitals. A gauge freedom results, which can be determined by the choice of $\langle\phi_i| i\partial_t |\phi_j\rangle$. According to [20], $\langle\phi_i| i\partial_t |\phi_j\rangle = h^i_j = \langle\phi_i| h |\phi_j\rangle$, where h is the one-particle Hamiltonian ($h = -\frac{1}{2}\nabla^2 - Z/r + V_{ext}$), is a numerically favourable choice. The resulting EOMs are given by

$$i\partial_t |\phi_p\rangle = h |\phi_p\rangle + QG |\phi_p\rangle + \sum_q |\phi_q\rangle R^q_p, \tag{3.12}$$

with the corresponding equations for the CI coefficients

$$i\partial_t C_I = \sum_J \langle\Phi_I| U |\Phi_J\rangle C_J. \tag{3.13}$$

In Equation 3.12, $Q = 1 - \sum_p |\phi_p\rangle\langle\phi_p|$ is the projection onto the virtual orbitals, i.e. all the orbitals which are neither frozen, dynamic, nor active orbitals. These orbitals have an occupation number of zero. R^q_p is the component of the time derivative of the orbitals within the occupied space, which is determined by the gauge. For $\langle\phi_i| i\partial_t |\phi_j\rangle = h^i_j$, $R^q_p = 0$, more details can be found in [20]. G contains the electron-electron interaction and is given by

$$G |\phi_p\rangle = \sum_{oqsr} \left(D^{-1}\right)^o_p D^{qs}_{or} U^r_s |\phi_q\rangle, \tag{3.14}$$

where $\left(D^{-1}\right)^o_p$ are elements of the inverse of the one-particle reduced density matrix, D^{qs}_{or} are elements of the two-particle reduced density matrix, and U^r_s is the matrix element of the Coulomb interaction

$$U^r_s(\mathbf{r}_1) = \int \frac{\phi^*_r(\mathbf{r}_2)\phi_s(\mathbf{r}_2)}{|\mathbf{r}_1 - \mathbf{r}_2|} d^3\mathbf{r}_2. \tag{3.15}$$

Implementation and time propagation

In a grid representation of the orbitals, exploiting the radial symmetry with respect to the nucleus, the $1/r_{12}$ term is numerically approximated using the multi-pole expansion given by [20]

$$\frac{1}{r_{12}} = \sum_{l=0}^{l_{2max}} \sum_{m=-l}^{l} \frac{4\pi}{2l+1} \frac{r_<^l}{r_>^{l+1}} Y_{lm}(\theta_1, \phi_1) Y_{lm}^*(\theta_2, \phi_2), \tag{3.16}$$

where Y_{lm} are the spherical harmonics, and $r_<$ and $r_>$ are the radii r_1 and r_2 depending on which one is larger. The expansion becomes exact for $l_{2max} = \infty$. In practice, l_{2max} is truncated at an appropriate level.

Furthermore, the ϕ orbitals are able to mix l quantum numbers as in

$$\left|\phi_p(t)\right\rangle = \sum_{l=0}^{l_{1max}} \varphi_p^l(t) \left|\chi_{lp}(t)\right\rangle, \tag{3.17}$$

where $\left|\chi_{lp}(t)\right\rangle$ is given in spatial coordinates as

$$\chi_{klm}(r,t,\theta,\phi) = R_{kl}(r,t) Y_{lm}(\theta,\phi), \tag{3.18}$$

where $R_{kl}(r,t)$ are the radial wave functions. The index p in Equation 3.17 enumerates the orbitals and separates into k and m. As the magnetic quantum number m is preserved [20], it is well suited as an orbital index. The presented equations of motion are a set of coupled nonlinear differential equations. Multiple suitable numerical propagators for this problems have been found and tested [32]. For the calculations presented below, an exponential Runge-Kuta propagator with Padé approximation for the time-evolution of the involved $\varphi-$ functions is used.

3.4. Methods based on reduced objects

HHG is an example, where the knowledge of a reduced object, in this case the particle density, is sufficient to gain full knowledge about the yield. In fact, the wave function for a multi-electron system contains an enormous amount of information that is practically never used directly for most experimentally relevant observables. Therefore, an obvious approach, to reduce the computational cost, is to propagate a simpler, reduced object instead the full wave function of a system. In the following, we will briefly discuss propagating the electron density within the time-dependent density-functional theory (TDDFT) and review the choice of the two-particle reduced-density matrix (2RDM) as a reduced object to propagate. For this purpose, we will first present the equations of motion for the 2RDM, followed by the discussion of the separation of the basis orbitals into active and core spaces within the TD2RDM method. Lastly, the stability of the method will be discussed and the purification scheme will be introduced.

3.4.1. Time-dependent density-functional theory

According to the Hohenberg-Kohn theorem, the density of the ground state of an interacting system is uniquely determined by the external potential and vice versa. The Runge-Gross theorem guarantees this bijective mapping also for time-dependent systems, and together with the van Leeuwen theorem this lays the basis for time-dependent density-functional theory (TDDFT). The van Leeuwen theorem states that for any two systems with the same initial state but different interactions there exist unique external potentials under which these systems have the same time evolution. Time-dependent Kohn-Sham DFT uses a reference system with negligible interactions whose wavefunction is build from a Slater determinant with orbitals ϕ_i and an external potential V_{KS}, which should produce the same time-dependent density as the physical system with electron-electron interactions. In practice, the equations of motion for the orbitals are chosen such that they satisfy

$$-\frac{1}{2}\nabla_i^2\phi_i + V_{KS}\phi_i = -\frac{1}{2}\nabla_i^2\phi_i + \big(V_a[\rho] + V_{ext}(t)[\rho] + V_H[\rho] + V_{xc}[\rho]\big)\phi_i = \varepsilon\phi_i, \tag{3.19}$$

where the Kohn-Sham potential V_{KS} is the sum of the Coulomb potential from the core V_a, the external potential $V_{ext}(t)$, the Hartree potential V_H, and an exchange-correlation potential V_{xc}. The first three terms are known functionals of the electronic density. As the theorems only guarantee the existence of a solution but do not give hints on an actual construction of a solution, an approximation needs to be made for the exchange-correlation potential. Different exchange-correlation functionals are suited for different problems and choosing it appropriately is important for DFT to achieve results comparable to more advanced methods. In this work we use the non-local GGA_C_LYP approximation for the exchange-correlation functional from the Libxc library [33]. Besides the problem of constructing equations of motion for the density within TDDFT, another problem is determining physical observables that are not simple functional of the density. For ionisation probabilities, e.g. we therefore resort to the Slater determinant ansatz within Kohn-Sham theory, which however inherits the problems of TDHF when it comes to the inherent interconnectedness of single- and double-ionisation. See [34] for more details.

3.4.2. Time-dependent two-particle reduced-density matrix method

The p-particle reduced-density-matrix (pRDM) is defined as the trace over all N-p particles of the density matrix

$$D_{1\ldots p} = \frac{N!}{(N-p)!}\mathrm{Tr}_{(p+1)\ldots N}[|\psi\rangle\langle\psi|], \tag{3.20}$$

where $N > p \geq 1$ is the number of particles and the trace $\mathrm{Tr}_{(p+1)\ldots N}$ describes the trace over all but p particles. Different normalisations are used in literature, and we will discuss some of them in chapter 4 of this thesis. The matrix representation of the pRDM in an orbital basis $\{\phi_u(t)\}_{u=1}^{N}$ is given as

$$D^{u_1\ldots u_p}_{v_1\ldots v_p} = \frac{N!}{(N-p)!} \sum_{\substack{u_{p+1}..u_N \\ v_{p+1}\ldots v_N}} \langle \phi_{v_1}..\phi_{v_N}|\psi\rangle \langle\psi|\phi_{u_1}..\phi_{u_N}\rangle . \tag{3.21}$$

Furthermore, from a pRDM the qRDM, with $p > q$, can be calculated by performing the partial trace

$$D_{1\ldots q} = \frac{(N-p)!}{(N-q)!} \mathrm{Tr}_{q+1\ldots p} D_{1\ldots p}. \tag{3.22}$$

One-particle reduced density matrix

Let us now look at the special cases of 1RDMs and their physical meaning. In the eigenbasis, the 1RDM can be written as

$$D_1 = \sum_i \lambda_i^{(1)} |\eta_i\rangle \langle\eta_i| , \tag{3.23}$$

where the eigenfunctions $|\eta_i\rangle$ are called natural orbitals and the eigenvalues $\lambda_i^{(1)}$ are the occupation numbers of those orbitals. Many physical observables relevant in attosecond and strong-field physics, such as the dipole moment or the dipole acceleration discussed in chapter 2, are single-particle observables. The expectation value of a single-particle observable O can be exactly calculated using only the 1RDM

$$\langle O\rangle = \langle\psi| O |\psi\rangle = \sum_i \lambda_i^{(1)} \langle\eta_i| O |\eta_i\rangle = \mathrm{Tr}_1[D_1 O]. \tag{3.24}$$

Two-particle reduced density matrix

In view of the above discussion it is tempting to use the 1RDM as the fundamental object to propagate. In fact corresponding theories have been developed (see e.g. [35]). However, the Hamiltonian of multi-electron atoms, Equation 3.1, features a two-particle operator, namely the Coulomb interaction between the electrons. Therefore, the energy of the system is also a two-particle operator and the 2RDM is needed to exactly calculate it. Furthermore, the two-particle ionisation probability discussed in chapter 6 is also a two-particle observable, when neglecting three-particle ionisation. In general, the structure of the Hamiltonian being a sum over single- and two-particle operators suggests that two-particle correlations are fundamentally important and should be included by resorting to the 2RDM as the reduced object of central interest. With the 2RDM, the total energy for a general multi-electron Hamiltonian that includes pairwise electron-electron interactions, can be evaluated as

$$E = \frac{1}{2} \mathrm{Tr}_{12}[D_{12}\bar{H}_{12}], \tag{3.25}$$

with the two-particle operator $\bar{H}_{12}$ given as

$$\bar{H}_{12} = \frac{h_1 + h_2}{N-1} + U_{12}, \tag{3.26}$$

where $U_{12} = 1/|\mathbf{r}_1 - \mathbf{r}_2|$ is the two-particle interaction and $h_i = -\frac{1}{2}\nabla_i^2 - Z/r_i + V_{ext}(\mathbf{r}_i)$ is the single-particle Hamiltonian.
The 2RDM can be written in cumulant expansion as

$$D_{12} = \mathcal{A}D_1D_2 + \Delta_{12} = D_{12}^{HF} + \Delta_{12}, \tag{3.27}$$

where Δ_{12} is the two-particle cummulant and $\mathcal{A}$ the antisymmetrisation operator acting on the 1RDMs as

$$\mathcal{A}D_1D_2 = D^{i_1}_{j_1}D^{i_2}_{j_2} - D^{i_1}_{j_2}D^{i_2}_{j_1}. \tag{3.28}$$

This is an analogy to the separation of the electron-pair density into a Hartree-Fock part and a correlation part [36]

$$\rho(\mathbf{r}_1, \mathbf{r}_2) = \rho^{HF}(\mathbf{r}_1, \mathbf{r}_2) + \rho^{c}(\mathbf{r}_1, \mathbf{r}_2). \tag{3.29}$$

We can associate the correlation pair-density ρ^c with the diagonal of the two-particle cummulant Δ_{12} in spatial coordinates. Hartree-Fock methods do not include the correlation part, which in atomic systems is smaller than the Hartree-Fock contribution. Post Hartree-Fock methods, like MCTDHF or TD2RDM, are necessary to include electron-electron correlations.

Symmetries and eigenspectrum of the 2RDM

Analogous to Equation 3.23 we can diagonalise the 2RDM

$$D_{12} = \sum_i \lambda_i^{(2)} |\gamma_i\rangle \langle\gamma_i|, \tag{3.30}$$

where the eigenvalues $\lambda_i^{(2)}$ are called geminal occupation numbers and $|\gamma_i\rangle$ are the geminals. As a basis for the 2RDM we choose spin orbitals. Therefore, the full 2RDM in space representation is given as

$$\begin{aligned}&\langle \mathbf{r}_1\mathbf{r}_2|D_{12}(t)\left|\mathbf{r}'_1\mathbf{r}'_2\right\rangle = \\ &\sum_{\substack{i_1,i_2,j_1,j_2\\ \sigma_{i_1},\sigma_{i_2},\sigma_{j_1},\sigma_{j_2}}} D^{i_1\sigma_{i_1}i_2\sigma_{i_2}}_{j_1\sigma_{j_1}j_2\sigma_{j_2}}(t)\phi^*_{i_1,\sigma_{i_1}}(\mathbf{r}_1,t)\phi^*_{i_2,\sigma_{i_2}}(\mathbf{r}_2,t)\phi_{j_1,\sigma_{j_1}}(\mathbf{r}'_1,t)\phi_{j_2,\sigma_{j_2}}(\mathbf{r}'_2,t).\end{aligned} \tag{3.31}$$

In general, using spin orbitals the full 2RDM can be written as

$$D^{u_1u_2}_{v_1v_2} = \begin{pmatrix} D^{i_1\uparrow i_2\uparrow}_{j_1\uparrow j_2\uparrow} & D^{i_1\uparrow i_2\uparrow}_{j_1\uparrow j_2\downarrow} & D^{i_1\uparrow i_2\uparrow}_{j_1\downarrow j_2\uparrow} & D^{i_1\uparrow i_2\uparrow}_{j_1\downarrow j_2\downarrow} \\ D^{i_1\uparrow i_2\downarrow}_{j_1\uparrow j_2\uparrow} & D^{i_1\uparrow i_2\downarrow}_{j_1\uparrow j_2\downarrow} & D^{i_1\uparrow i_2\downarrow}_{j_1\downarrow j_2\uparrow} & D^{i_1\uparrow i_2\downarrow}_{j_1\downarrow j_2\downarrow} \\ D^{i_1\downarrow i_2\uparrow}_{j_1\uparrow j_2\uparrow} & D^{i_1\downarrow i_2\uparrow}_{j_1\uparrow j_2\downarrow} & D^{i_1\downarrow i_2\uparrow}_{j_1\downarrow j_2\uparrow} & D^{i_1\downarrow i_2\uparrow}_{j_1\downarrow j_2\downarrow} \\ D^{i_1\downarrow i_2\downarrow}_{j_1\uparrow j_2\uparrow} & D^{i_1\downarrow i_2\downarrow}_{j_1\uparrow j_2\downarrow} & D^{i_1\downarrow i_2\downarrow}_{j_1\downarrow j_2\uparrow} & D^{i_1\downarrow i_2\downarrow}_{j_1\downarrow j_2\downarrow} \end{pmatrix}, \tag{3.32}$$

where the indices $\{i, j\}$ refer to spatial orbitals with ↑ for spin up and ↓ for spin down, while $\{u, v\}$ refer to spin orbitals. As the fermionic wave function is anti-symmetric, $D^{u_1u_2}_{v_1v_2}$ is anti-symmetric under permutation of either the upper or the lower indices. Due to this symmetry many entries in Equation 3.32 are 0 and the 2RDM simplifies to

$$D^{u_1u_2}_{v_1v_2} = \begin{pmatrix} D^{i_1\uparrow i_2\uparrow}_{j_1\uparrow j_2\uparrow} & 0 & 0 & 0 \\ 0 & D^{i_1\uparrow i_2\downarrow}_{j_1\uparrow j_2\downarrow} & D^{i_1\uparrow i_2\downarrow}_{j_1\downarrow j_2\uparrow} & 0 \\ 0 & D^{i_1\downarrow i_2\uparrow}_{j_1\uparrow j_2\downarrow} & D^{i_1\downarrow i_2\uparrow}_{j_1\downarrow j_2\uparrow} & 0 \\ 0 & 0 & 0 & D^{i_1\downarrow i_2\downarrow}_{j_1\downarrow j_2\downarrow} \end{pmatrix}. \tag{3.33}$$

In the following, we will restrict ourselves to total spin singlet systems, where $S^2 = S_z^2 = 0$. In this case, only the $D^{i_1\uparrow i_2\downarrow}_{j_1\uparrow j_2\downarrow}$ block needs to be calculated and all other contributions can be reconstructed from it [37]. This block will be called the up-down-block in the following. Its cummulant expansion is given by

$$D^{i_1\uparrow i_2\downarrow}_{j_1\uparrow j_2\downarrow} = D^{i_1\uparrow}_{j_1\uparrow}D^{i_2\downarrow}_{j_2\downarrow} + \Delta^{i_1\uparrow i_2\downarrow}_{j_1\uparrow j_2\downarrow}. \tag{3.34}$$

Furthermore, from the eigenvalues of the up-down-block, we can reconstruct the eigenvalues of the full 2RDM using symmetries. As the $D^{i_1\uparrow i_2\uparrow}_{j_1\uparrow j_2\uparrow}$ and $D^{i_1\downarrow i_2\downarrow}_{j_1\downarrow j_2\downarrow}$ are anti-symmetric under permutation of either the upper or lower indices, the eigenvalues corresponding to anti-symmetric eigenstates of the up-down-block appear three times in the full eigenvalue spectrum while the ones corresponding to symmetric eigenstates appear only once. The up-down-block has also symmetric eigenvalues, as the anti-symmetry can be restored by the spin component, which is not possible for the other two blocks. Besides that, all the eigenvalues of the up-down-block need to be multiplied by 2 to get the correct value for the full 2RDM because all four blocks with up- and down-spin have the same eigenvalues.

2RDM in second quantisation

The 2RDM has an interesting connection to two-particle Green's functions, which can be most easily seen using second quantisation. We will give only an example for the 2RDM in second quantisation but the same works for arbitrary pRDMs. When starting from a vacuum state $|0\rangle$ the creation operator $a_u^\dagger$ creates one electron in the u-th orbital and the annihilation operator a_v annihilates an electron in the v-th orbital. When the annihilation operator acts on a state, where the orbital in which the electron is supposed to be annihilated is empty, the result is zero. The same holds for the creation operator, when the orbitals is already occupied. With this, the 2RDM is given as

$$D^{u_1u_2}_{v_1v_2} = \langle\Psi| a^\dagger_{u_1} a^\dagger_{u_2} a_{v_2} a_{v_1} |\Psi\rangle \,. \tag{3.35}$$

The entries of the 2RDM can therefore be interpreted as the overlap between a state where v_1 and v_2 have been annihilated and a state where u_1 and u_2 have been annihilated.

The BBGKY hierarchy and time propagation

For the time propagation of the 2RDM, we use time-dependent orbitals as a basis following the approach within MCTDHF. We chose the equations of motion for the orbitals to be identical to the ones for TD-CASSCF described in subsection 3.3.3. Furthermore, the same gauge freedom for $\langle\phi_i| i\partial_t |\phi_j\rangle$ remains. For time-propagation, it is again advantageous to choose $\langle\phi_i| i\partial_t |\phi_j\rangle = h^i_j$, but in section 5.1, a different choice is discussed.
The EOM for the 2RDM is determined based on the EOM for the full density matrix $D_{1\ldots N}$, i.e. using the von-Neumann-Lioville equation

$$i\partial_t D_{1\ldots N} = [H_{1\ldots N}, D_{1\ldots N}], \tag{3.36}$$

where $H_{1\ldots N}$ is the full N-particle Hamiltonian. By partially tracing out all but two particles, we get the equation of motion for D_{12}

$$i\partial_t D_{12} = [H_{12}, D_{12}] + \mathrm{Tr}_3[U_{13} + U_{23}, D_{123}], \tag{3.37}$$

where D_{123} is the 3RDM. With the Hamiltonian given in Equation 3.3, the EOMs for the orbitals and 2RDM, using the gauge $\langle\phi_i|\, i\partial_t\, |\phi_j\rangle = h^i_j$, can be written as

$$i\partial_t\, |\phi_p\rangle = h\, |\phi_p\rangle + Q \sum_{oqsr} \left(D^{-1}\right)^o_p D^{qs}_{or} U^r_s\, |\phi_p\rangle\,, \tag{3.38}$$

$$i\partial_t D_{12} = [U_{12}, D_{12}] + \mathrm{Tr}_3[U_{13} + U_{23}, D_{123}]. \tag{3.39}$$

Equivalently, the time evolution of the 3RDM requires the knowledge of the 4RDM and so on. This finding is known as the Bogoliubov-Born-Green-Kirkwood-Yvon (BBGKY) hierarchy. Obviously, the EOM for the 2RDM is not closed and cannot be used as such. Any practical application requires a closure, where the 3RDM has to be expressed as a functional of the 2RDM at least in an approximate way. In the following we will call this process reconstruction.

Reconstruction

Exploiting the cummulant expansion for the 3RDM

$$D_{123} = \mathcal{A} D_1 D_2 D_3 + \mathcal{A} D_{12} D_3 + \Delta_{123}, \tag{3.40}$$

we obtain explicit dependencies on the 1RDM and 2RDM. But there remains the unknown contribution from the three-particle cummulant Δ_{123}, for which there are different approximations. The Valdemoro reconstruction simply sets it to zero, while in the Mazziotti reconstruction [38] the cummulant expansion of the 4RDM is employed and by setting $\mathrm{Tr}_4[\Delta_{1234}]$ to zero, Δ_{123} can be reconstructed. For the calculations presented in this thesis, the Nakatsuji-Yasuda (NY) reconstruction [39], [19] is used. Within this reconstruction by using a diagrammatic expansion, two classes of diagrams, which contribute to Δ_{123} can be calculated. Furthermore, we enforce symmetries on the reconstructed cummulant [37], [19], [31], which are not already satisfied by the reconstruction functional. We enforce contraction consistency (CC), for the whole 3RDM as well as for separate spin-blocks, which means that the trace of the 3RDM (or its parts) must give the 2RDM with appropriate normalisations. This results in particle number and energy conservation for general CC and conservation of spin for the CC of the spin-blocks.

TD2RDM and CASSCF

Similarly to the TD-CASSCF method presented in subsection 3.3.3 we want to use a separation of the orbitals into active and core orbitals within the TD2RDM method. The

2RDM then has entries with orbitals from the active space, as well as from the core space

$$D^{u_1 u_2}_{v_1 v_2} = \begin{pmatrix} D^{u_{c1} u_{c2}}_{v_{c1} v_{c2}} & D^{u_{c1} u_{c2}}_{v_{c1} v_{a2}} & D^{u_{c1} u_{c2}}_{v_{a1} v_{c2}} & D^{u_{c1} u_{c2}}_{v_{a1} v_{a2}} \\ D^{u_{c1} u_{a2}}_{v_{c1} v_{c2}} & D^{u_{c1} u_{a2}}_{v_{c1} v_{a2}} & D^{u_{c1} u_{a2}}_{v_{a1} v_{c2}} & D^{u_{c1} u_{a2}}_{v_{a1} v_{a2}} \\ D^{u_{a1} u_{c2}}_{v_{c1} v_{c2}} & D^{u_{a1} u_{c2}}_{v_{c1} v_{a2}} & D^{u_{a1} u_{c2}}_{v_{a1} v_{c2}} & D^{u_{a1} u_{c2}}_{v_{a1} v_{a2}} \\ D^{u_{a1} u_{a2}}_{v_{c1} v_{c2}} & D^{u_{a1} u_{a2}}_{v_{c1} v_{a2}} & D^{u_{a1} u_{a2}}_{v_{a1} v_{c2}} & D^{u_{a1} u_{a2}}_{v_{a1} v_{a2}} \end{pmatrix}, \tag{3.41}$$

where the indices *ci* refer to core orbitals and *ai* to active orbitals. In second quantisation, Equation 3.35, it becomes clear that all matrix elements, which have a different number of active and core indices in either the upper or lower indices, e.g. $D^{u_{a1} u_{a2}}_{v_{a1} v_{c2}}$, have to be zero. In other words, there can not be an overlap between a wave function, which has had one electron from the core orbitals annihilated and the same wave function which has had no electron from its core orbitals annihilated. Ten of the sixteen contributions in Equation 3.41 are, therefore, zero.

When considering $D^{u_{c1} u_{c2}}_{v_{c1} v_{c2}}$, we know that the Hartree-Fock like fully occupied core orbitals cannot account for any correlation. Therefore, this block separates into 1RDMs with the two-particle cummulant being zero. Furthermore, all core orbitals have their occupation fixed to one, such that the 1RDM of core orbitals is trivially given by the Dirac-delta δ^i_j as

$$D^{u_{c1} u_{c2}}_{v_{c1} v_{c2}} = \mathcal{A} D^{u_{c1}}_{v_{c1}} D^{u_{c2}}_{v_{c2}} = \mathcal{A} \delta^{u_{c1}}_{v_{c1}} \delta^{u_{c2}}_{v_{c2}}. \tag{3.42}$$

The contributions from the four blocks, which each have one active and one core orbital index in the upper and lower indices, i.e. $D^{u_{c1} u_{a2}}_{v_{c1} v_{a2}}$, $D^{u_{c1} u_{a2}}_{v_{a1} v_{c2}}$, $D^{u_{a1} u_{c2}}_{v_{c1} v_{a2}}$ and $D^{u_{a1} u_{c2}}_{v_{a1} v_{c2}}$, can all be reproduced by only one of them, when exploiting the anti-symmetry under permutation of either the upper or lower indices

$$D^{u_{c1} u_{a2}}_{v_{c1} v_{a2}} = D^{u_{a2} u_{c1}}_{v_{a2} v_{c1}} = -D^{u_{c1} u_{a2}}_{v_{a2} v_{c1}} = -D^{u_{a2} u_{c1}}_{v_{c1} v_{a2}}. \tag{3.43}$$

Furthermore, for these blocks the two-particle cummulant has to be zero as well, as two of its indices refer to core orbitals with vanishing correlations. The 1RDM for the core elements $D^{u_{c1}}_{v_{c1}}$ is again a Dirac-delta as all core orbitals are fully occupied such that the cummulant decomposition of these matrices amounts to

$$D^{u_{c1} u_{a2}}_{v_{c1} v_{a2}} = D^{u_{c1}}_{v_{c1}} D^{u_{a2}}_{v_{a2}} = \delta^{u_{c1}}_{v_{c1}} D^{u_{a2}}_{v_{a2}}. \tag{3.44}$$

When all indices refer to active orbitals, no simplifications can be made. The resulting element includes correlations in the two-particle cummulant

$$D^{u_{a1} u_{a2}}_{v_{a1} v_{a2}} = \mathcal{A} D^{u_{a1}}_{v_{a1}} D^{u_{a2}}_{v_{a2}} + \Delta^{u_{a1} u_{a2}}_{v_{a1} v_{a2}}. \tag{3.45}$$

At the end, out of the sixteen blocks of the full 2RDM, only one block given in Equation 3.45 does not reduce to single particle contributions. Therefore, for the EOM of the 2RDM, only the part, which describes pairs in active orbitals needs to be propagated. All the other terms can be reconstructed by contracting the 2RDM to the 1RDM and combining it with Dirac-deltas for the core orbitals. This separation thus allows us, to significantly reduce the size of the 2RDM.

Stability and purification

As the reconstruction discussed above is not exact, the positive-semi-definiteness of the 2RDM can be violated during time propagation [37]. This is clearly unphysical. In general, the question, which conditions a 2RDM has to fulfil to guarantee the existence of an N-body wavefunction that contracts to it, is still open. However, a constructive method exists to find necessary conditions [40].

Empirically, it has been found previously that the time propagation becomes unstable as the lowest eigenvalues of the 2RDM become negative. This problem can be remedied by iteratively "correcting" the 2RDM. This procedure is called purification [37]. It should be noted that the purification is applied a-posteriori after the propagation step and is not part of the EOMs. Despite the fact that purification works usually well, there are cases where the purification fails, and no stable propagation is possible. Furthermore, if the calculations need too many purification steps, the quality of the results deteriorates.

The purification in its present form violates energy conservation. An energy conserving purification scheme has been suggested in [41], but has not been implemented yet. Therefore, all calculations presented in this thesis are done with non-energy conserving purification. This is only a minor issue in the present case of weakly correlated multi-electron atoms but becomes more important as correlations increase.

4. Measures of correlation and entanglement

The field of quantum information theory has developed a plethora of measures for correlation and entanglement, however, most are assuming distinguishable particles/subsystems [42]. These measures of correlation and entanglement cannot be easily transferred to indistinguishable fermionic systems [21]. In quantum information theory, a state ρ_0 is called uncorrelated when the expectation value of any local observable in one subsystem is independent of the expectation value in the other subsystems. For example for two uncorrelated subsystems with density matrices $\rho_{A/B}$ and observables A and B the expectation value for both observables can be written as

$$\langle AB \rangle_{\rho_0} = \langle A \rangle_{\rho_A} \langle B \rangle_{\rho_B}. \tag{4.1}$$

When this separation is not possible, the state is called correlated and the measure of correlation gives the distance to the closest uncorrelated state. If the state is a mixture of uncorrelated states $\rho = \sum_i c_i \rho_0^{(i)}$, with coefficients c_i, it is called separable or non-entangled. Otherwise the state is called entangled and the relative entropy of entanglement determines how close the state is to the closest non-entangled state.
In systems of indistinguishable fermions, however, the simplest antisymmetrised state of two electrons $|ab\rangle = |a\rangle |b\rangle - |b\rangle |a\rangle$ is by the above definition correlated. Therefore, the measure of interest for a fermionic state is how close it is to a Hartree-Fock state. In the following, we will discuss a few such measures.

4.1. Pure vs. mixed states

From statistical physics we know that for a pure state the density matrix is given by

$$\rho = |\psi\rangle \langle\psi| , \tag{4.2}$$

where $|\psi\rangle$ is the full wave function. If the system consists of a mixture of different states, the density matrix is given by

$$\rho = \sum_i p_i |\psi_i\rangle \langle\psi_i| , \tag{4.3}$$

where p_i is the probability for the system to be in the state $|\psi_i\rangle$. As $\mathrm{Tr}[\rho] = 1$, $\sum p_i = 1$ must hold as well. If $i = 1$, Equation 4.3 for the mixed state goes over into Equation 4.2 for the pure state. Furthermore, $\rho^2 = \rho$ for a pure state, but not for a mixed state. Therefore, $1 - \mathrm{Tr}\left[\rho^2\right]$ works as a measure of how close a state is to a pure state.
To be able to apply this measure also for reduced density matrices, we have to take their normalisation into account. We want to normalise our pRDMS such that $\mathrm{Tr}\left[D^2_{1\ldots p}\right] = 1$ for a Hartree-Fock sate. If the pRDMs are normalised to one, as density matrices usually are, the purity for the Hartree-Fock pRDM would give the inverse of the number of non-zero eigenvalues $\binom{N}{p}^{-1}$. In contrast, our pRDMs, as presented in section 3.4, are normalised as $\mathrm{Tr}[D_{1\ldots p}] = \frac{N!}{(N-p)!}$, therefore the purity of a Hartree-Fock state is given by $\frac{N!p!}{(N-p)!}$. To obtain $\mathrm{Tr}\left[D^2_{1\ldots p}\right] = 1$ for a Hartree-Fock state, we therefore must normalise to $\binom{N}{p}$. This allows for comparison of purity between systems with different electron numbers. In the following we will use the mixedness of a state, which we define as

$$m(D_{1\ldots p}) = 1 - \mathrm{Tr}\left[D^2_{1\ldots p}\right], \tag{4.4}$$

where the pRDM is normalised to $\binom{N}{p}$. As the trace is basis independent, we can simply compute the mixdness in the eigenbasis, where it is sufficient to know the eigenspectrum of the pRDM.

4.2. Entropy

A widely used measure for correlation is the entropy. We will use the von Neumann entropy

$$S(\rho) = \mathrm{Tr}[\rho \log(\rho)], \tag{4.5}$$

which can be defined for the one- and two-particle RDM as

$$S_1(D_1) = \mathrm{Tr}[D_1 \log(D_1)], \tag{4.6}$$
$$S_2(D_{12}) = \mathrm{Tr}[D_{12} \log(D_{12})]. \tag{4.7}$$

The measure is independent of the basis and it is sufficient to know the eigenvalues of the 1RDM and 2RDM, to calculate it. In order for the entropy of Hartree-Fock states to be 0, the pRDM is again normalised to $\binom{N}{p}$. Compared to probability theory, where entropies are evaluated for distributions normalised to one, this normalisation leads to a shift and rescaling of the entropy. Since we are mostly interested in the dynamical behaviour of the entropy and its usage as a measure of deviation from a the Hartree-Fock state, this is of no concern.

4.3. Direct measures from the TD2RDM method

A direct way of measuring the deviation from a Hartree-Fock state, and thereby the electron-electron correlations, can be found by the cumulant expansion Equation 3.27 of the 2RDM

$$D_{12} = \mathcal{A} D_1 D_2 + \Delta_{12} = D_{12}^{HF} + \Delta_{12}, \tag{4.8}$$

where all correlations are captured by the two-particle cummulant. Therefore, the two-particle cummulant is a natural measure for the correlation within the TD2RDM method. The Frobenius norm, or Schatten 2-norm, of the two-particle cummulant

$$||\Delta_{12}|| = \sqrt{\mathrm{Tr}\left[\Delta_{12}^{\dagger}\Delta_{12}\right]}, \tag{4.9}$$

has already been used as a time-dependent correlation measure [43] [44]. It can be easily computed as

$$||\Delta_{12}|| = \sqrt{\sum_i \sum_j \sum_k \sum_l \left|(\Delta_{12})_{ij}^{kl}\right|^2}. \tag{4.10}$$

5. Preparation of the ground state

In order to calculate the time-evolution for HHG, a stable ground state is needed. As the TD2RDM equations of motion differ from the MCTDHF ones, Equation 3.37, we cannot simply calculate the ground state of the system by imaginary time-propagation as it is done for MCTDHF. A TD2RDM ground state could be calculated, e.g. by adiabatic switching, where starting from a Hartree-Fock state, the electronic correlations are adiabaticly switched on. As this is not yet implemented, we take the MCTDHF ground states, which are ground states of the exact multi-particle Hamiltonian and the MCTDHF EOMs but not of the EOMs for the D_{12} with the approximated three-particle cumulant. In order to make the ground state more stable under the TD2RDM equations of motion, a procedure, which we call averaging, has been developed [19]. We review and evaluate the procedure of averaging in detail here.

5.1. Equation of motion and propagator

Within the procedure of averaging the 2RDM from the MCTDHF ground state is averaged over a field-free TD2RDM time propagation of duration T. The averaged 2RDM is then obtained as

$$\overline{D^{u_1u_2}_{v_1v_2}} = \frac{1}{T}\int_0^T D^{u_1u_2}_{v_1v_2}(t)dt. \tag{5.1}$$

For the averaging of the initial state we take the orbitals to be fixed and only propagate the 2RDM. Based on this, we choose the gauge for the equations of motion to be

$$\langle\phi_i|\, i\partial_t\, |\phi_j\rangle = 0, \tag{5.2}$$

such that the equation of motion for the 2RDM in this case reads as

$$i\partial_t D_{12} = [h_1 + h_2, D_{12}] + [W_{12}, D_{12}] + \mathrm{Tr}_3[W_{13} + W_{23}, D_{123}]. \tag{5.3}$$

Equation 5.3 differs from Equation 3.38, used for propagation in a field, by the gauge choice Equation 5.2. The single-particle part of the Hamiltonian is transformed from the orbitals equation of motion to the 2RDM equation of motion. The orbitals are not propagated during averaging. The scaling of the computational effort for the averaging is thus independent of the spatial grid and the orbitals of the averaged ground state do not differ from the initial ones.

5.2. Reasons for averaging

To understand why we need the averaging procedure of the initial state let us compare TD2RDM calculations performed with averaged and not averaged MCTDHF ground states to the results within the MCTDHF method. In Figure 5.1, we plot the dipole acceleration during HHG for different driving laser fields for beryllium, neon, and argon. For all calculations a sin^2 envelope is used for the laser pulse. The field parameters for beryllium and neon are chosen to match those from [19] and for the argon calculations [45] is used as a reference, where i.e. we use a 2 cycle, 800 nm, $I = 4 \times 10^{14}\mathrm{W\,cm^{-2}}$ laser pulse. Especially for beryllium, the not-averaged ground state within TD2RDM gives an unphysical result with very high oscillations. In comparison, the dipole acceleration using the averaged initial state within TD2RDM is in good agreement with the MCTDHF calculations.
For neon a 2 cycle, 800 nm, and $I = 1 \times 10^{15}\mathrm{W\,cm^{-2}}$ driving field is used. Here the oscillations from the not-averaged initial state are much smaller, even though they are still noticeable, especially at the beginning and the end of the pulse, where the dipole acceleration is small for the TD2RDM with averaged initial state and MCTDHF calculation. The latter two, again, are in good agreement.
For argon a 3 cycle, 780 nm, and $I = 3.5 \times 10^{14}\mathrm{W\,cm^{-2}}$ driving field is used. Here, very good agreement between all three calculations is observed, with the only discrepancy appearing between the 3rd and 4th optical cycle when the laser is already off, where the dipole acceleration for the TD2RDM calculation with the not-averaged ground state slightly differs from the other two calculations.
In general, we observe that the averaging of the ground state becomes less important the heavier the atoms are and the more electrons they have. This can be associated with the relative correlation energy becoming smaller in comparison with the total energy of the atom as the atomic number increases. As the treatment of the correlations is the only source of error within the TD2RDM method, this is plausible.

For further analysis of these oscillations in the dipole acceleration, let us look at the spectrum of the dipole acceleration, i.e. the HHG yield. In Figure 5.2, we can see the harmonic yields for the beryllium, neon and argon calculations. Starting from argon we see good agreement between all three calculations for the whole range of the spectrum. For neon the agreement is good for the first 15 harmonic orders, then the yield calculated within TD2RDM from the not-averaged ground state shows marked deviations. Nevertheless, the overall shape is similar and the cut-off is clearly visible. In contrast, the harmonic spectrum for the TD2RDM calculation of beryllium with the not-averaged ground state shows strong deviations from MCTDHF, which grow with harmonic order. In contrast, using an averaged ground state, we observe excellent agreement with MCTDHF. In addition the spurious oscillations when using the not-averaged ground state show up especially at higher frequencies and thus bear the risk of overlaying the cut-off. This is especially visible in the neon spectrum.

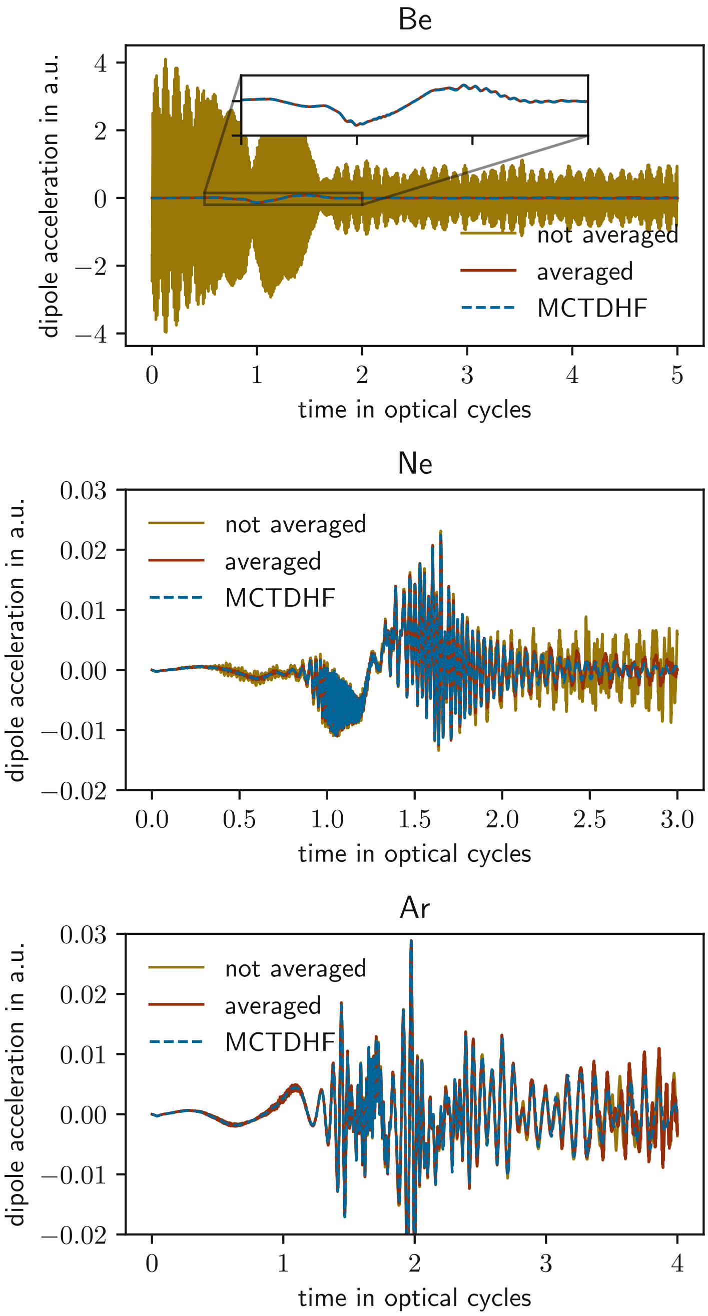

Figure 5.1: Dipole acceleration for HHG in beryllium, neon and argon. The plots show TD2RDM results for averaged and not averaged MCTDHF ground states, as well as MCTDHF calculations. For beryllium we have used a 2 cycle, 800 nm laser pulse with $I = 4 \times 10^{14}\,\mathrm{W\,cm^{-2}}$, for neon 2 cycles, 800 nm, and $I = 1 \times 10^{15}\,\mathrm{W\,cm^{-2}}$, and for argon 3 cycles, 780 nm, and $I = 3.5 \times 10^{14}\,\mathrm{W\,cm^{-2}}$.

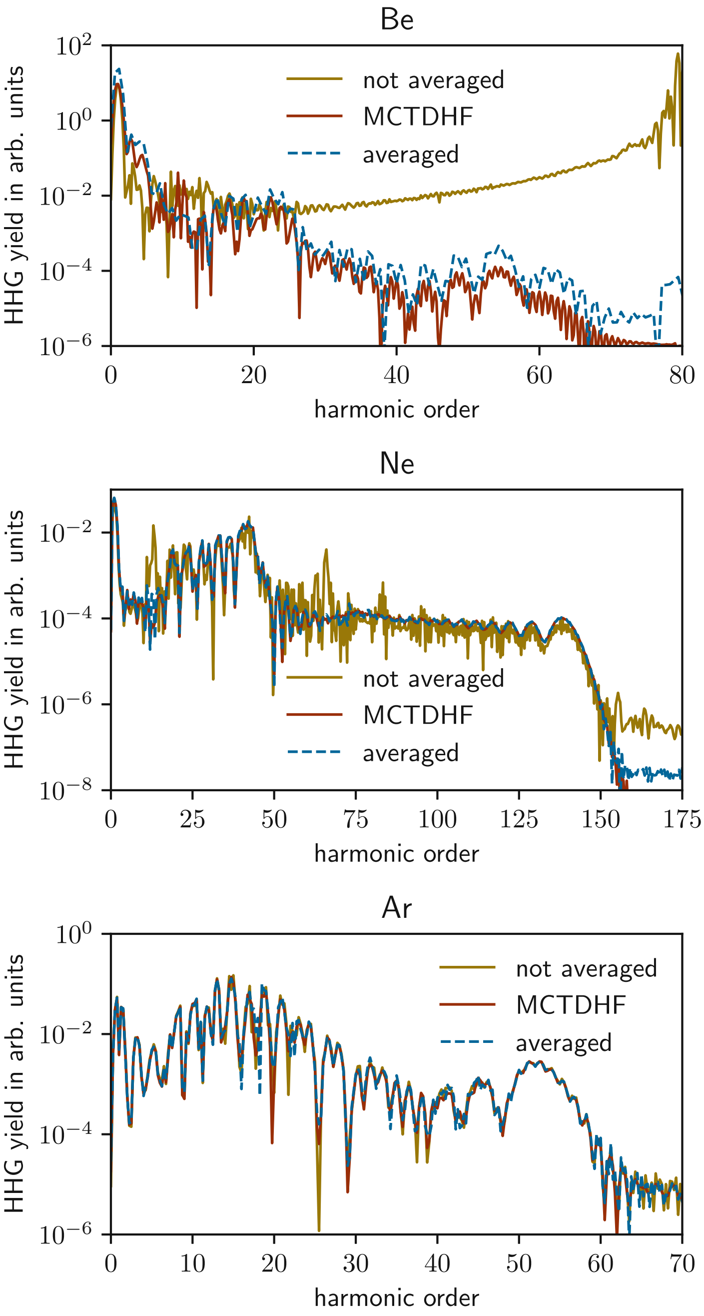

Figure 5.2: HHG yield in beryllium, neon and argon. The plots show TD2RDM results for averaged and not averaged MCTDHF ground states, as well as MCTDHF calculations. For beryllium we have used a 2 cycle, 800 nm laser pulse with $I = 4 \times 10^{14}\mathrm{W\,cm^{-2}}$, for neon 2 cycles, 800 nm, and $I = 1 \times 10^{15}\mathrm{W\,cm^{-2}}$, and for argon 3 cycles, 780 nm, and $I = 3.5 \times 10^{14}\mathrm{W\,cm^{-2}}$.

5.3. Changes on the 2RDM due to the averaging

As we have seen, the initial state preparation through averaging is essential within the TD2RDM method to achieve physical results. Let us now investigate in more detail, the effect of this procedure on the ground state from which we start the calculations. As an example we look at the beryllium state, because it has the least orbitals and is therefore the easiest to visualise. In Figure 5.3 we can see the up-down-block of the linearised 2RDM, i.e. both upper indices run horizontally, while both lower indices run vertically from one to the number of orbitals, e.g. the lower index 21, and upper index 32, corresponds to the entry D^{32}_{21} of the 2RDM. In this way we can display the four dimensional 2RDM as a two dimensional matrix. We see that the largest contributions are on the diagonal for the highest occupied orbitals, 1s and 2s. Here we plot the real part of the 2RDM on a linear colour-scale as well as the absolute value on a logarithmic colour-scale, to highlight smaller entries of the 2RDM. The 2RDM obtained from the MCTDHF ground-state calculations has only real valued entries.

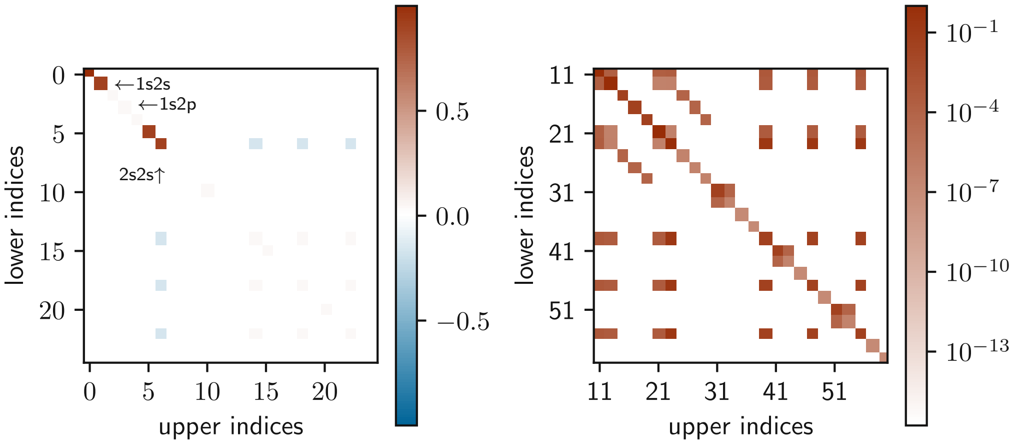

Figure 5.3.: Real part of the linearised up-down-block of the 2RDM of the beryllium ground state on a linear colour-scale and absolute value of the up-down-block on a logarithmic colour-scale, with 1s, 2s and 2p orbitals as a basis.

In Figure 5.4, we can see the real and imaginary part of the difference of the 2RDM

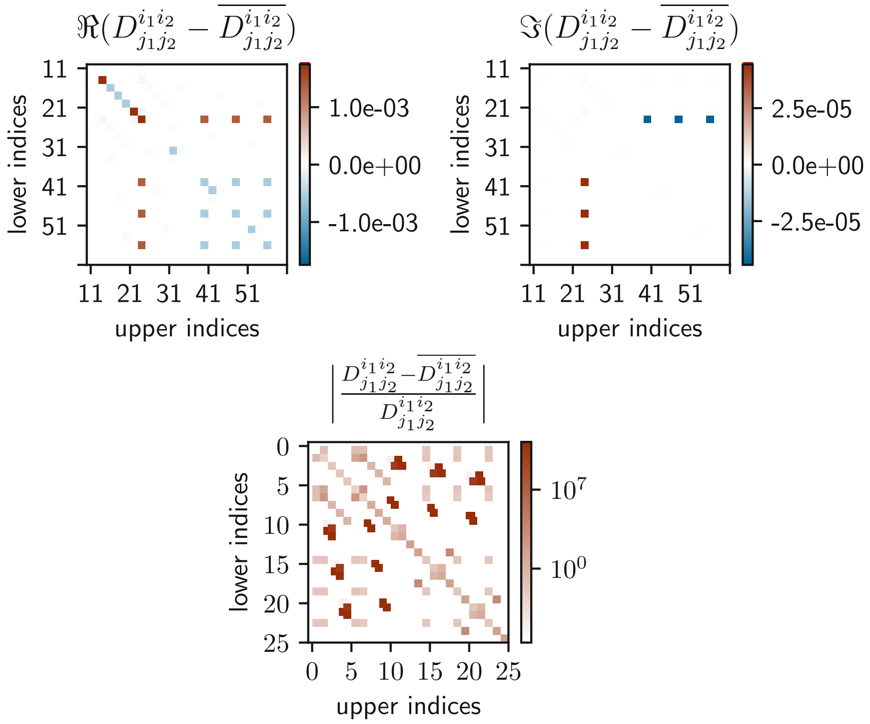

Figure 5.4.: Real and imaginary part of the difference between the values in the up-down-block of the 2RDM for beryllium before and after averaging. For the relative difference we choose a logarithmic colour scale and plot the absolute value of the matrix elements.

before and after the averaging $(D^{i_1i_2}_{j_1j_2} - \overline{D^{i_1i_2}_{j_1j_2}})$. Before averaging, the state is purely real but through the averaging we also get an imaginary contribution. The 2RDM stays Hermitian and the imaginary part is relatively small. Furthermore, the absolute value of the relative difference

$$\frac{D^{i_1i_2}_{j_1j_2} - \overline{D^{i_1i_2}_{j_1j_2}}}{D^{i_1i_2}_{j_1j_2}}, \tag{5.4}$$

for each element is plotted and a logarithmic colour scale is used in order to highlight also smaller changes. Overall, we observe that some diagonal elements get smaller while several off-diagonal elements increase. This indicates, that the 2RDM gets more mixed. To quantify this effect we present in Table 5.1 the mixedness of the 2RDM as well as the 1RDM. Using the normalisation to $\binom{N}{p}$ as discussed in section 4.1 allows us to better compare values for different atoms. Overall, we observe that all RDMs get more mixed by the averaging except for the 1RDM of neon. Furthermore, the 1RDMs are generally purer than the 2RDMs, which is most probably just the effect of a larger number of entries being unequal to one in the 2RDM compared to the 1RDM. We would expect the

	Be	Ne	Ar with core	Ar
1RDM				
mixedness before averaging	0.09108467	0.00815775	0.01096783	0.00049386
mixedness after averaging	0.09259254	0.00815759	0.01107941	0.00049417
2RDM				
mixedness before averaging	0.12144576	0.01440403	0.02056182	0.00092944
mixedness after averaging	0.12344275	0.01440436	0.02076761	0.00093003

Table 5.1.: Purity of the 1- and 2RDM of the beryllium, neon, and argon ground states before and after averaging. The averaging enhances the mixedness of the state.

purity to increase with the atomic number as the correlation energy decreases. The fact, that this is not the case for neon and argon here originates from using the separations into active and core orbitals for argon, but not for neon. This effect vanishes when the argon calculations are done without core orbitals, i.e. all orbitals are set to active.

6. Correlation effects during high harmonic generation

In this chapter, we investigate electronic correlation effects during high harmonic generation. Starting with results already presented in [19], which we reproduce here as a numerical check, we apply the correlation measures discussed in chapter 4. We observe different regimes of the dynamical build-up of correlations, which we investigate further by varying the laser parameters. We start our discussion with beryllium, and successively investigate larger atoms, i.e. neon and argon. In Appendix B preliminary results on xenon are presented. We provide all relevant input parameters for the numerical results presented here, in Appendix A.

6.1. Beryllium

Following [19] we start with a 2 cycle, 800 nm, $4 \cdot 10^{14}\,\mathrm{W\,cm^{-2}}$ driving laser. In Figure 6.1, the resulting dipole acceleration as well as the electrical field strength of the laser field are plotted. We compare TDHF, TDDFT, MCTDHF and TD2RDM calculations. The latter two are in excellent agreement with each other. The difference to the TDHF and TDDFT calculations is not significant when only looking at the dipole acceleration.

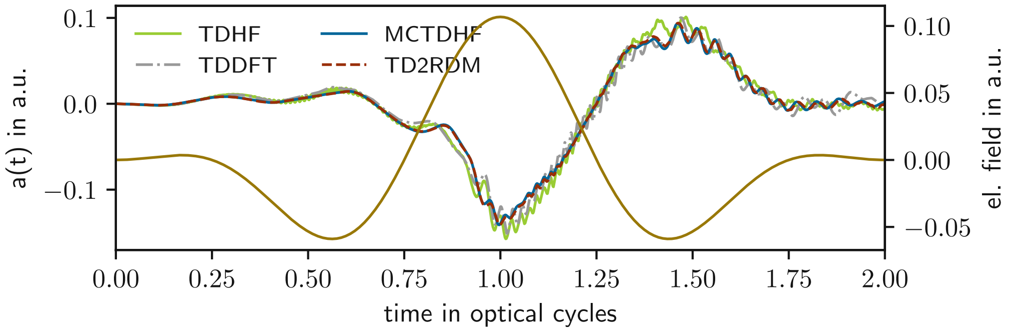

Figure 6.1.: Dipole acceleration for HHG in beryllium within TDHF, TDDFT, MCTDHF and TD2RDM. The electrical field of the 2 cycle, 800 nm, and $I = 4 \times 10^{14}\ \mathrm{W\,cm^{-2}}$ laser pulse is plotted in dark yellow.

In contrast, the HHG yield calculated from the dipole acceleration according to Equation 2.6 (see Figure 6.2) shows strong deviations for the yield close to the cut-off within TDHF and TDDFT. The MCTDHF and TD2RDM calculations are in excellent agreement with each other.

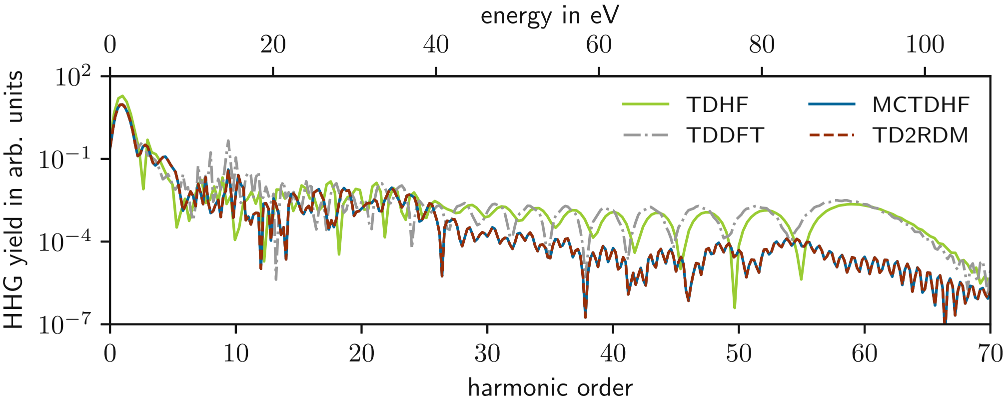

Figure 6.2.: HHG spectrum for beryllium within TDHF, TDDFT, MCTDHF and TD2RDM, with the same laser parameters as in Figure 6.1.

We know apply the correlation measures from chapter 4 to these results, see Figure 6.3. For better comparison, all measures are normalised to their initial value $\frac{f(t)}{f(0)}$. Additionally, also the electrical field of the laser field is plotted. We observe that all the measures which take either the 1RDM or the 2RDM as input are equivalent under this normalisation (the difference being of the order of 1×10^{-5}), see Figure 6.3. Importantly, all measures show the same temporal behaviour: At approximately 0.5 optical cycles, the correlation first decreases, followed by a steep increase at the time of the maximal field strength at 1 optical cycle. After that all measures show oscillations around an almost constant value. These results show that qualitatively and partly also quantitatively these measures contain the same information on dynamical correlation effects. Due to their similarity, we will restrict our analysis to one of the measures, i.e. the Frobenius norm of the two-particle cummulant as it has the most largest range, i.e. the largest amplitude compared to its initial value, of all discussed measures and is also the most natural measure for the TD2RDM method. Consistent with the observation in chapter 5 the ground state of beryllium is more mixed than for neon and argon, we observe that the ground state of beryllium is also the most correlated one out of those three.

In order to gain a better understanding of the process, the upper panel in Figure 6.4 shows the occupation numbers of the natural orbitals, i.e. the eigenvalues of the 1RDM. For beryllium, at first only the 1s and 2s orbitals are occupied, while the 2p orbitals are practically unoccupied. During the process of HHG, electrons from the 2s orbital get ionised to the previously empty 2p $m_s = \pm 1$ orbitals. During this process the l quantum number

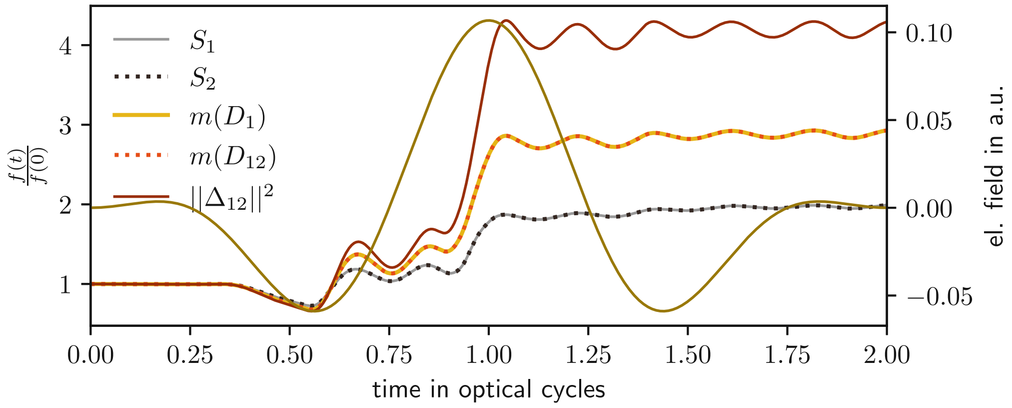

Figure 6.3.: Correlation measures normalised to their initial value. We compare the entropy and purity of the 1RDM and 2RDM with the Frobenius norm of the two-particle cummulant from the MCTDHF calculations. The laser parameters are the same as in Figure 6.1.

looses its meaning, as the orbitals mix to other l states. At about 0.5 optical cycles, all the 2p orbitals get depleted into 2s, which explains the reduction in correlation we observe at this time, as this increases the purity of the RDM. In general, the original 2p $m_s = 0$ orbital has a lower occupation at the end than in the beginning. It is also remarkable that the time dependence of the third largest eigenvalue of the 1RDM represents quite well the time dependence of the correlation measures. Furthermore, the agreement between MCTDHF and TD2RDM is very good also for the prediction of occupation numbers.

In the middle panel of Figure 6.4 the one- and two-particle ionisation probabilities are plotted. To obtain the ionisation probabilities, we integrate the electron density for the one-particle ionisation, and the electron-pair density for the two-particle ionisation outside a given radius R_{ion}, which we set to R_{ion} = 20 a.u. for the calculations presented in this thesis. The exact time dependency of the ionisation probabilities depend on this radius during the laser pulse (the steps in ionisation probability are shifted in time towards larger values when we increase R_{ion}), but the final ionisation probability is converged. For further technical details on the calculation of the ionisation probabilities we refer to [15]. In the present case of beryllium with with $I_p \approx 9$ eV [26] and the Keldysh parameter being $\gamma \approx 0,485$, the one- and two-particle ionisation probabilities are quite high.

To further assess the quality of the TD2RDM results we plot the Frobenius norms of the two-particle cummulants within MCTDHF and TD2RDM in the third panel of Figure 6.4. The two methods show good agreement during the first optical cycle, but start to deviate afterwards. As the two methods only differ by the three-particle cumulant entering the TD2RDM, this discrepancy can be attributed to the inaccurate description of three-particle correlations within the TD2RDM method. The discrepancies are more prominent in the two-particle cummulant of the up-down block than in the up-up block.

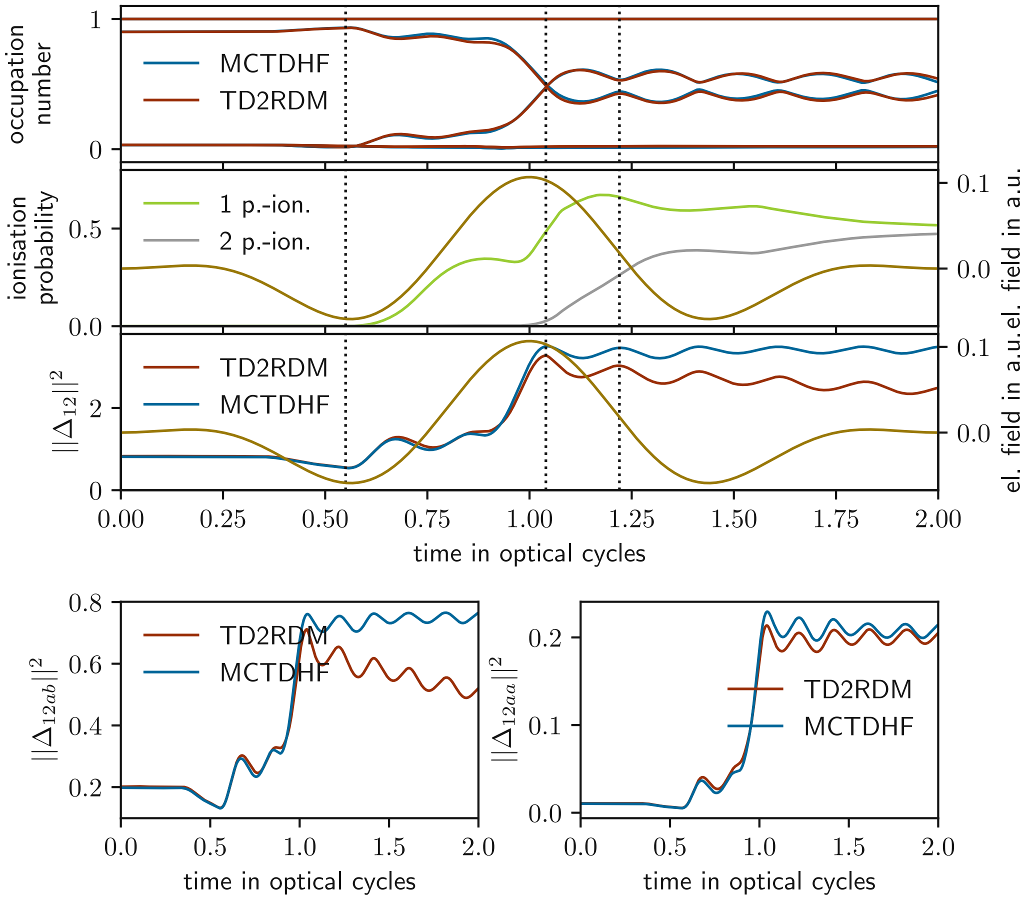

Figure 6.4.: The first panel shows the natural occupation numbers, i.e. eigenvalues of the 1RDM within MCTDHF and TD2RDM for beryllium. The second panel shows the one- and two-particle ionisation probabilities respectively. The third panel shows the Frobenius norm of the two-particle cummulant within MCTDHF and TD2RDM. The last two panels show the norm of the up-down and up-up block of the two-particle cummulant. The electrical field of the 2 cycle, 800 nm, and $I = 4 \times 10^{14}\ \mathrm{W\,cm^{-2}}$ laser pulse is plotted in dark yellow.

In general, the contribution form the up-down block, which corresponds to electron-pairs with opposite spin, is larger than the contribution from the up-up block, which corresponds to electron-pairs of same spin. The maxima in the cummulant after 1 optical cycle correspond to points in time when the occupation numbers from the 2s and 2p orbitals are the closest. At this points, the 1RDM is also the most mixed, thus most correlated.

We now turn to a parameter regime of weaker laser fields to suppress tow-particle ionisation while at the same time increasing the wavelength of the laser field to reach approximately the same cut-off as before. Specifically, we present calculations with a 2 cycle, 2000 nm, and $I = 5 \times 10^{13}$ W cm^{-2} laser pulse, i.e. a Keldysh parameter of $\gamma \approx 0.50$. We observe very good agreement between the MCTDHF and TD2RDM calculations also in this regime, see Figure 6.5. The deviations within the TDHF and TDDFT calculations from MCTDHF are already prominent in the dipole acceleration. The HHG spectrum in Figure 6.6 confirms the excellent agreement between the MCTDHF and TD2RDM results and the discrepancies to TDHF and TDDFT.

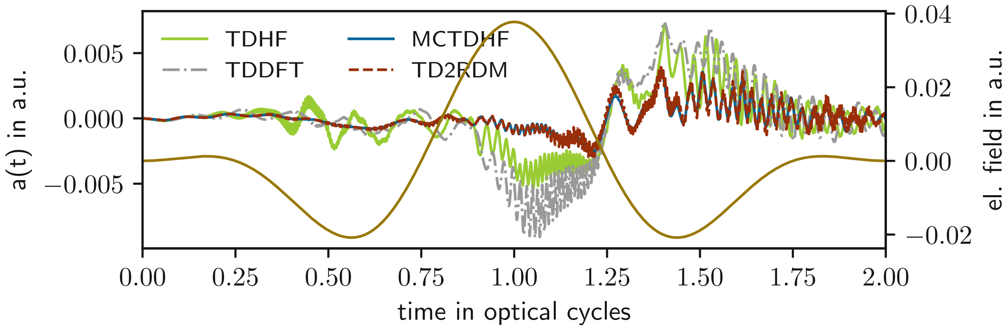

Figure 6.5.: Dipole acceleration for HHG in beryllium within TDHF, TDDFT, MCTDHF and TD2RDM. The electrical field of the 2 cycle, 2000 nm, and $I = 5 \times 10^{13}$ W cm^{-2} laser pulse is plotted in dark yellow.

The one-particle ionisation probability in the central panel of Figure 6.7 reaches 10%, while the two-particle ionisation probability is negligible. An interesting behaviour is observed in the time dependence of the natural occupation numbers in the upper panel of Figure 6.7. Here we see a depletion of the already weakly occupied 2p orbitals during the first two large amplitude modulations of the laser field, at around 0.55 and 1.05 optical cycles. TD2RDM reproduces this behaviour very well.

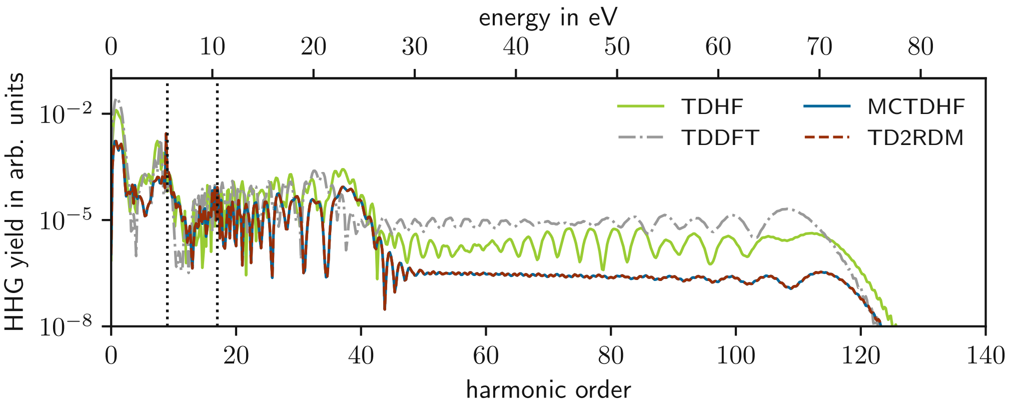

Figure 6.6.: HHG spectrum for beryllium within TDHF, TDDFT, MCTDHF and TD2RDM, with the same laser field parameters as in Figure 6.5.

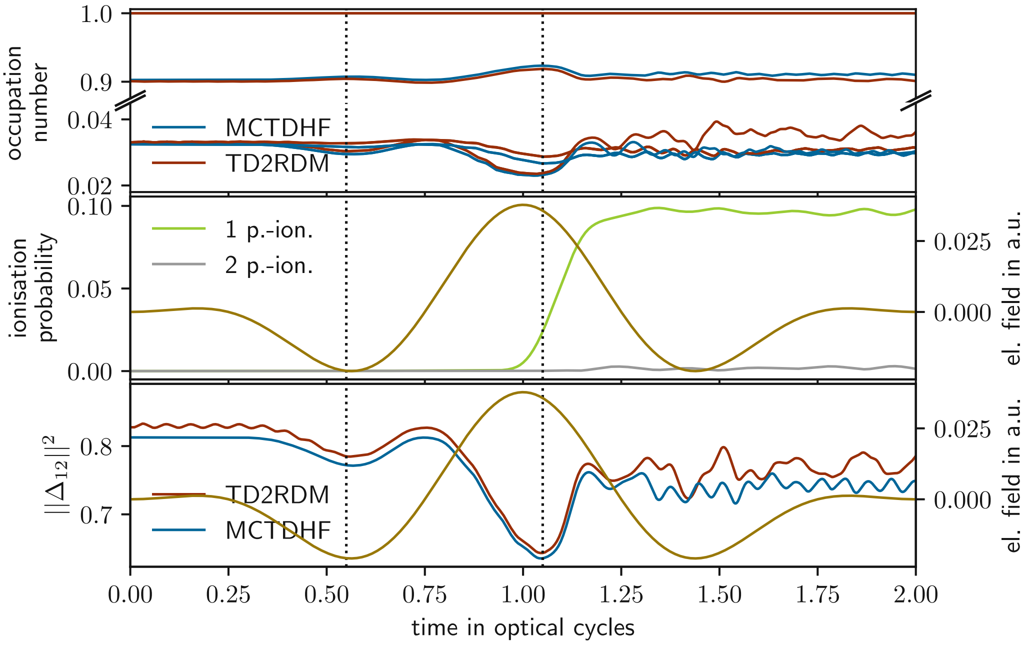

Figure 6.7.: The upper panel shows the natural occupation numbers, i.e. eigenvalues of the 1RDM within MCTDHF and TD2RDM for beryllium. The central panel shows the one- and two-particle ionisation probabilities respectively. The lower panel shows the Frobenius norm of the two-particle cummulant within MCTDHF and TD2RDM. The electrical field of the 2 cycle, 2000 nm, and $I = 5 \times 10^{13}\ \mathrm{W\,cm^{-2}}$ laser pulse is plotted in dark yellow.

This translates into decreasing two-particle correlations during the process of HHG as is shown in the lower panel of Figure 6.7. TD2RDM slightly overestimates the correlations compared to MCTDHF. Interestingly, the two-particle correlations remain reduced at the end of the pulse. This originates from the fact that the final system is closer to a Hartree-Fock state than the initial ground state such that the initially quite strongly occupied orbitals obtain even more weight.

We now perform a windowed Fourier transform (Gabor transform) of both the dipole acceleration in Figure 6.5 as well as the two-particle cummulant in Figure 6.7, using the *specgram* function of *matplotlib* [46] with the Blackman window. While $a(t)$ is a single-particle observable, Δ_{12} is a two-particle observable directly sensitive to correlated two-particle dynamics, e.g. two-particle resonances. It is therefore interesting to compare the spectral features in both observables. We observe that frequency components from the second plateau at high harmonic orders, larger than 50, which originate from the ionisation at small intensities at the first large laser field modulation and recombination at large intensities at the second large amplitude modulation, are strongly suppressed within $||\Delta_{12}||^2$. This indicates that two-particle correlations are not relevant here. The situation changes for the second plateau starting at 1 laser cycle. Here, large contributions at approximately the 19th harmonic order are visible in both the HHG yield as well as in the two-particle cummulant, see Figure 6.6 (vertical lines) and Figure 6.8 (horizontal lines).Interestingly, we observe a constant frequency structure in the Gabor transform of $||\Delta_{12}||^2$ starting with the first optical cycle, which might indicate the presence of a two-particle resonance. The structure is similar to single-particle resonances observed in the time-frequency analysis of $a(t)$ in lithium [47]. A similar structure is present in the HHG yield, however, at slightly smaller frequencies of about 9 harmonic orders, and could indicate the presence of a single-particle resonance. Both spectral features are marked in the HHG yield in Figure 6.6, as they are both prominently visible. We will investigate these features in more detail in follow-up studies.

In the Gabor transform for the beryllium calculations with the 2 cycle, 800 nm, and $I = 4 \times 10^{14}\ \mathrm{W\,cm^{-2}}$ laser pulse no such features were visible. The structures we found here are all within the energy range of the first five harmonics, see Figure 6.2, and are thus not well resolved in this case.

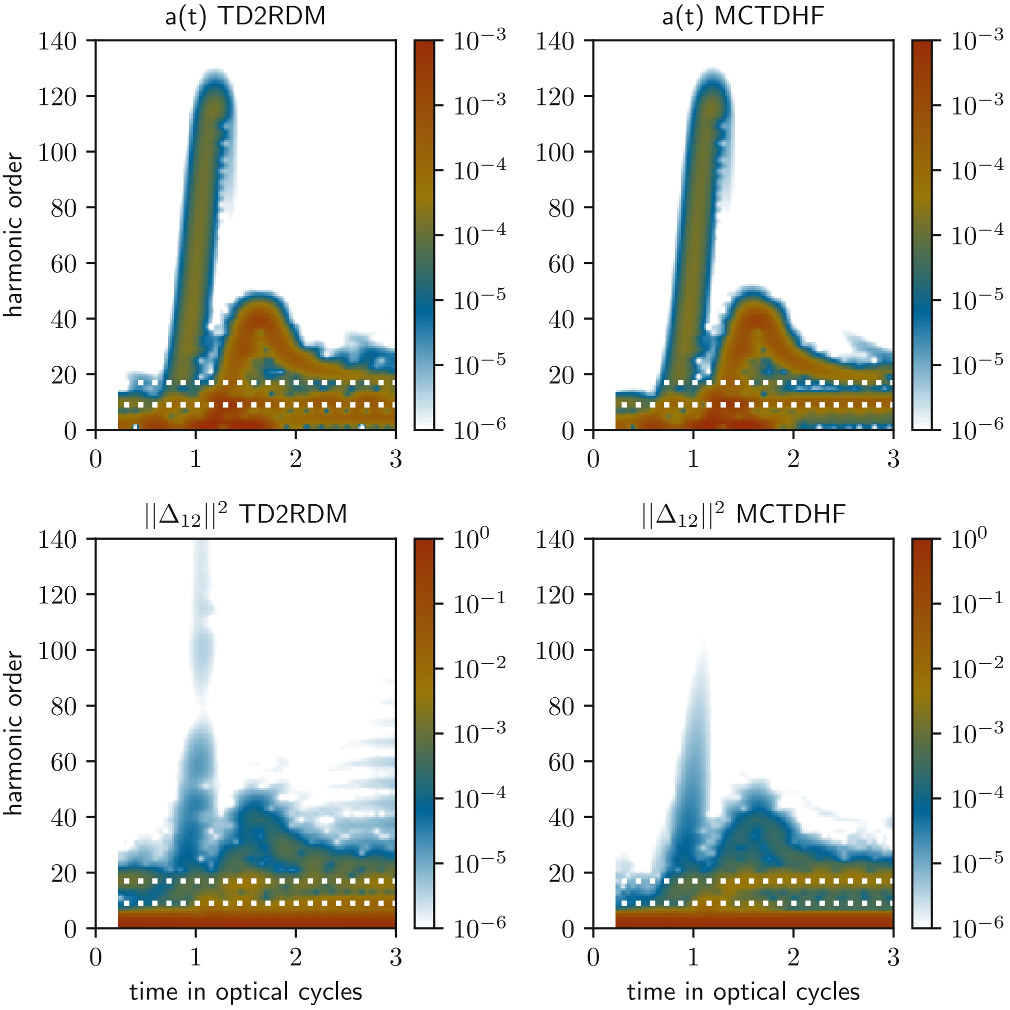

Figure 6.8.: Time-frequency analysis of the dipole acceleartion and two-particle cummulant within TD2RDM and MCTDHF calculations for beryllium. The laser parameters are 2 cycles, 2000 nm, and $I = 5 \times 10^{13}\ \mathrm{W\,cm^{-2}}$.

In order to further analyse the correlations for high harmonic orders, we repeat the beryllium calculations with a longer laser pulse of 4 optical cycles. The results are only shown for the MCTDHF calculation, see Figure 6.9. As there are now long trajectories, which start from an already partly ionised atom, the harmonics at high orders show more correlation compared to Figure 6.8. The spectral feature at the 19th harmonic order is also present for this case.

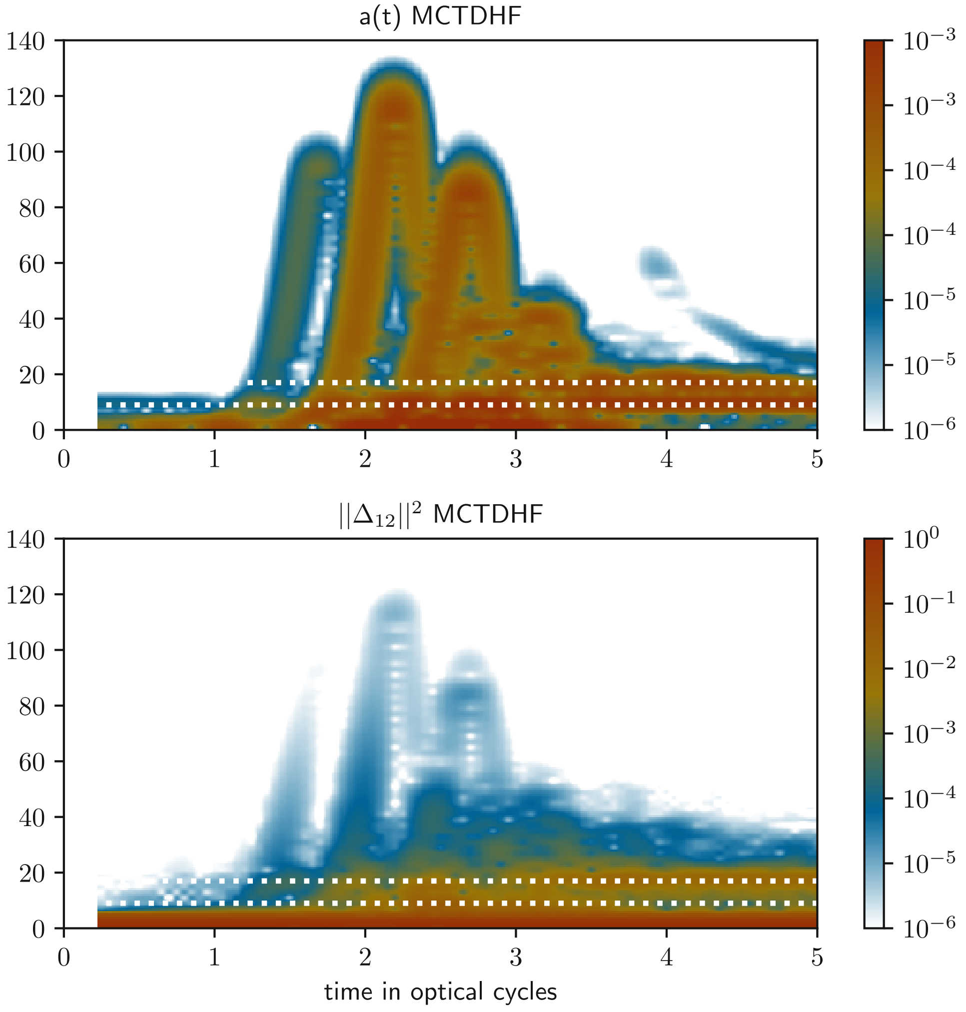

Figure 6.9.: Time-frequency analysis of the dipole acceleration and two-particle cummulant within MCTDHF calculations for beryllium. The laser parameters are 4 cycles, 2000 nm, and $I = 5 \times 10^{13}\ \mathrm{W\,cm^{-2}}$.

6.2. Neon

We now investigate HHG in neon with a 2 cycle, 800 nm, and $10^{15}\mathrm{W\,cm^{-2}}$ driving laser field, following [19]. This seemingly high laser intensity results in low ionisation probabilities comparable to the second calculation from section 6.1, as neon has a high ionisation potential of 21.56 eV [26]. Furthermore, with a Keldysh parameter of $\gamma \approx 0.43$ we are in a similarly strong field regime. Figure 6.10 shows the resulting dipole acceleration within the TDDFT, TDHF, MCTDHF and TD2RDM calculations as well as the amplitude of the electrical field of the driving laser. Again, we see very good agreement between the MCTDHF and TD2RDM methods. The dipole acceleration obtained by the TDHF calculation is also comparable in shape and size, while TDDFT gives a substantially different result.

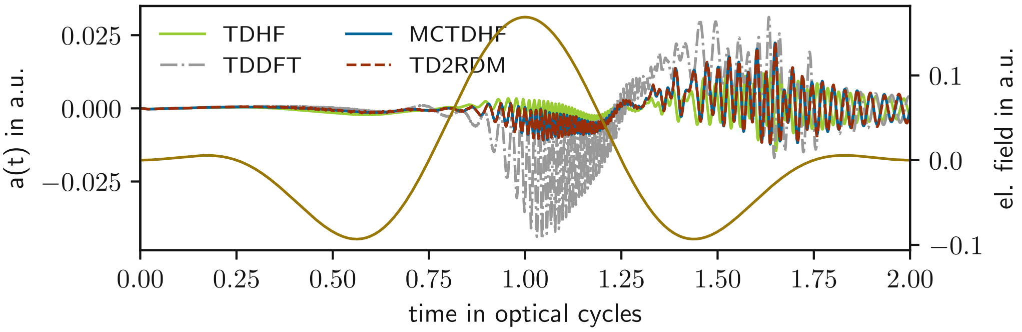

Figure 6.10.: Dipole acceleration in neon within TDHF, TDDFT, MCTDHF and TD2RDM. The electrical field of the 2 cycle, 800 nm, and $I = 1 \times 10^{15}\ \mathrm{W\,cm^{-2}}$ laser pulse is plotted in dark yellow.

These discrepancies are also visible in the HHG spectrum, Figure 6.11, where TDDFT shows the largest deviations from the MCTDHF benchmark. Similarly to the beryllium results, the spectra are in good agreement for lower frequencies, while the harmonic yield is vastly different for higher frequencies. All four methods predict the same cut-off frequency.

The one- and two-particle ionisation probabilities, see the central panel of Figure 6.12, are comparable to the ones for beryllium in Figure 6.7 in their temporal behaviour as well as their magnitude.

The shape of the laser field is imprinted on the occupation numbers as well as the two-particle cummulant, see Figure 6.12, where local maxima are slightly time-delayed compared to the large amplitude modulations of the laser field. We see clear traces of the three-step model, where e.g. after one optical cycle we see effects of recombination by an increase of the occupations of the highly occupied orbitals after previous depletion. In general the occupation numbers obtained by both methods (MCTDHF and TD2RDM) are in good agreement with each other.

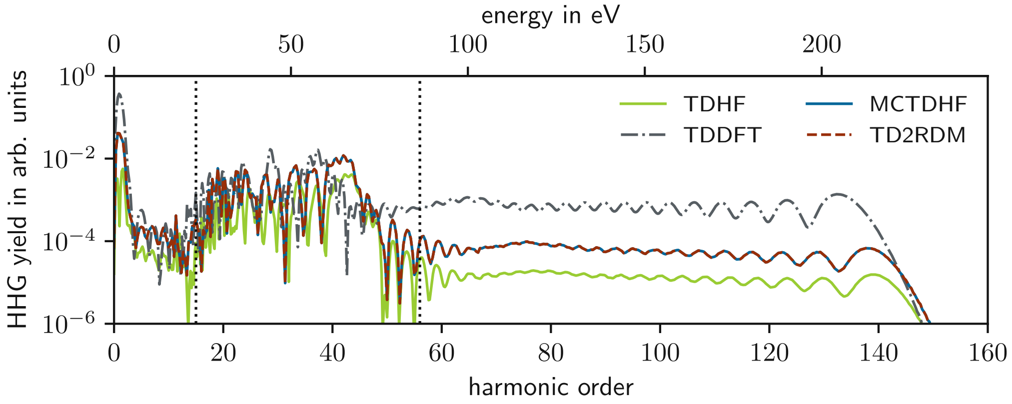

Figure 6.11.: HHG spectrum for neon within TDHF, TDDFT, MCTDHF and TD2RDM, with the same laser field parameters as in Figure 6.10.

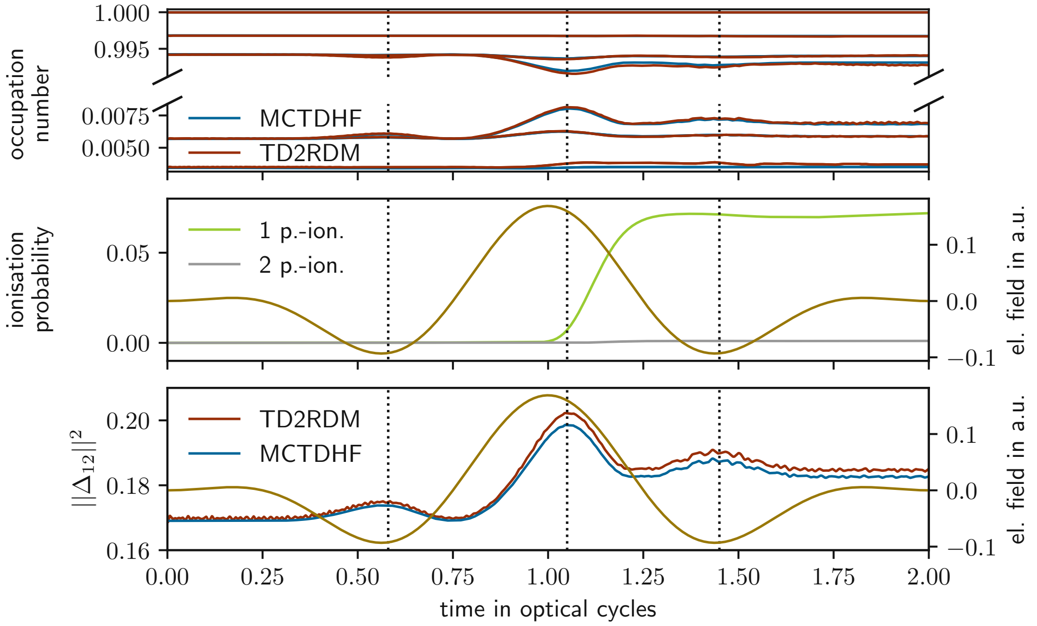

Figure 6.12.: The upper panel shows the natural occupation numbers, i.e. eigenvalues of the 1RDM within MCTDHF and TD2RDM for neon. The central panel shows the one- and two-particle ionisation probabilities respectively. The lower panel shows the Frobenius norm of the two-particle cummulant within MCTDHF and TD2RDM. The electrical field of the 2 cycle, 800 nm, and $I = 1 \times 10^{15}\ \mathrm{W\,cm^{-2}}$ laser pulse is plotted in dark yellow.

The qualitative agreement between the time dependence of the occupation numbers and the two-particle cummulant is also present in this case. Overall, the neon atom shows less correlations than beryllium. We see a qualitatively different time behaviour of the correlations. Firstly, we do not see any decrease in correlations below the ground-state value. After the highest increase, which again occurs at the time of the highest field intensity, there is a decrease in correlation again. The final value at the end of the laser pulse is larger than at the beginning. This might be due to the finite residual ionisation of the atom. The TD2RDM slightly overestimates the two-particle correlations and has additional noise compared to the results from MCTDHF.

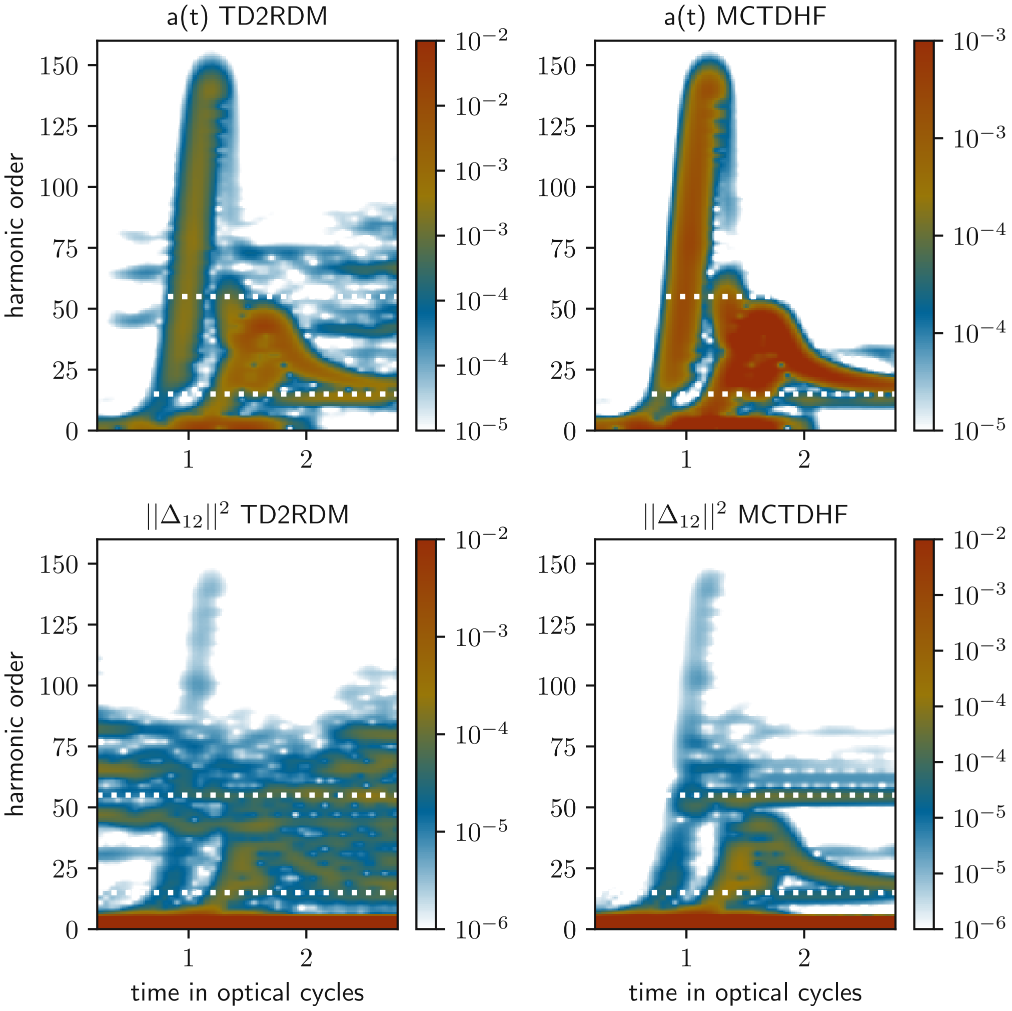

Figure 6.13.: Time-frequency analysis of the dipole acceleration and two-particle cummulant within TD2RDM and MCTDHF calculations for neon. The same laser parameters as in Figure 6.10 are used.

This is also visible in the time-frequency analysis of the dipole acceleration as well as the two-particle cummulant in Figure 6.13. There, the higher harmonic orders exhibit less correlations, while the harmonics from the second lower energy plateau are more correlated. We observe a prominent frequency component at approximately the 55th harmonic order in the spectrum of the Frobnenius norm of the two-particle cummulant which is most likely responsible for the enhancement at the end of the first lobe in the Gabor transform of $a(t)$, see Figure 6.13. A second feature around the 15th harmonic order is visible in both the dipole acceleration as well as the Frobenius norm of the two-particle cummulant. Both features are, however, not easily recognisable in the HHG spectrum, see Figure 6.11. We will investigate these features in more detail in follow up studies.

6.3. Argon

Finally, we want to present results for argon, where the separation into core and active spaces for the electrons is employed. One of the interesting features that might influence the HHG yield is the Cooper minimum. The Cooper minimum was first predicted by John Cooper for argon and krypton [48]. For argon it appears as a minimum in the photo ionisation probabilities at approximately 50 eV. It originates from the sign change in the dipole matrix element between the bound outer p orbitals and the unbound d orbitals. This spectral feature can be observed in HHG [45] as recombination is governed by the same matrix element. We have analysed the process of HHG in argon with a three cycle laser field at 780 nm and $I = 3.5 \times 10^{14}$ $\mathrm{W\,cm^{-2}}$, following [45]. With argon having an ionisation probability of 15.75 eV [26], this gives a Keldysh parameter of $\gamma \approx 0.63$. In the following, we directly compare this parameter regime to one with a stronger field of $I = 8 \times 10^{14}$ $\mathrm{W\,cm^{-2}}$, which gives a Keldysh parameter of $\gamma \approx 0.41$. Having the same system driven with two different laser intensities allows us to directly compare two different parameter regimes and observe the influence of the laser intensity on the dynamic behaviour of the correlation measures.

Figure 6.14 shows the dipole acceleration for both intensities obtained within the TDHF, TDDFT, TDCASSCF and TD2RDM methods. For the lower intensity, we observe good agreement between the TDHF, TDCASSCF and TD2RDM methods while the TDDFT calculations show the largest discrepancy. For the higher intensities the TDCASSCF and TD2RDM method show slight discrepancies, especially at the end of the laser pulse. The source of this discrepancy could be the accumulation of error due to the reconstructed three-particle cummulant during the longer propagation times.

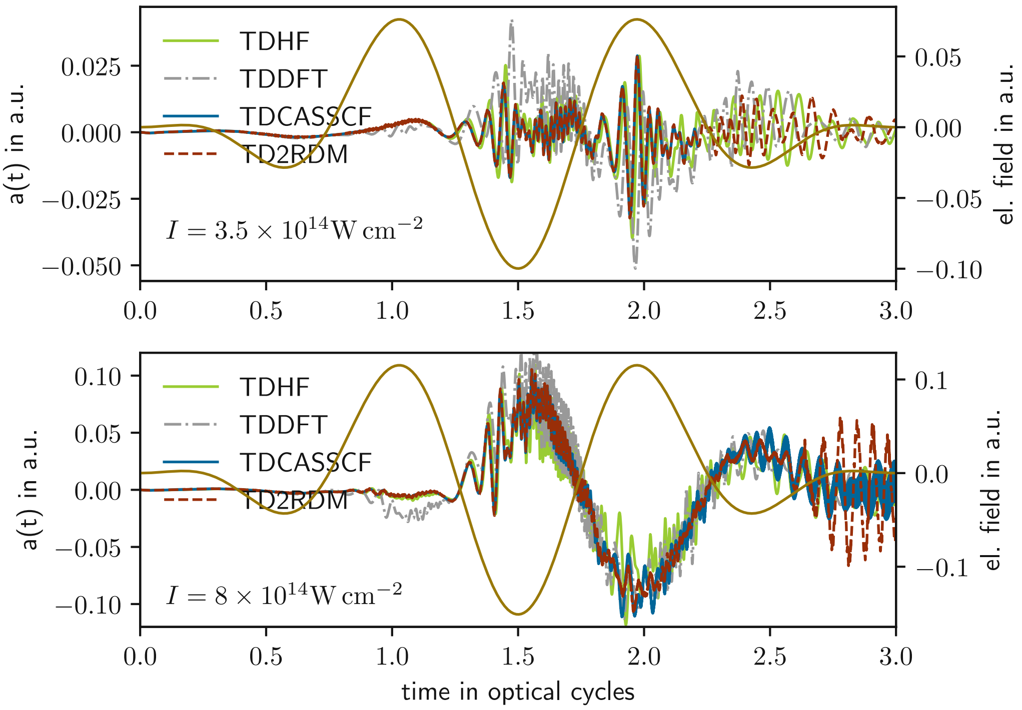

Figure 6.14.: Dipole acceleration for HHG in argon driven with a 3 cycle, 780 nm and $I = 3.5 \times 10^{14}$ W cm^{-2} and $I = 8 \times 10^{14}$ W cm^{-2} laser pulse. The results are obtained within TDHF, TDDFT, TDCASSCF and TD2RDM. Additionally the electrical field is plotted in dark yellow.

The HHG spectra obtained from the TDCASSCF and TD2RDM calculations are in good agreement with each other, see Figure 6.15. For the lower intensity laser field all three spectra obtained from TDHF, TDCASSCF and TD2RDM are in good agreement with each other, while at high intensities, the spectra obtained from the TDDFT calculations most strongly differ from the one obtained from TDCASSCF calculations. For both cases the Cooper minimum is clearly visible at around 55 eV (there seems to be a slight shift towards higher energies for $I = 3.5 \times 10^{14}$ W cm^{-2} and lower energies for $I = 8 \times 10^{14}$ W cm^{-2}). For the lower intensity, our findings are in good agreement with the measurements presented in [45] even though the minimum obtained from our calculations is not as deep as the one obtained in the experiment.

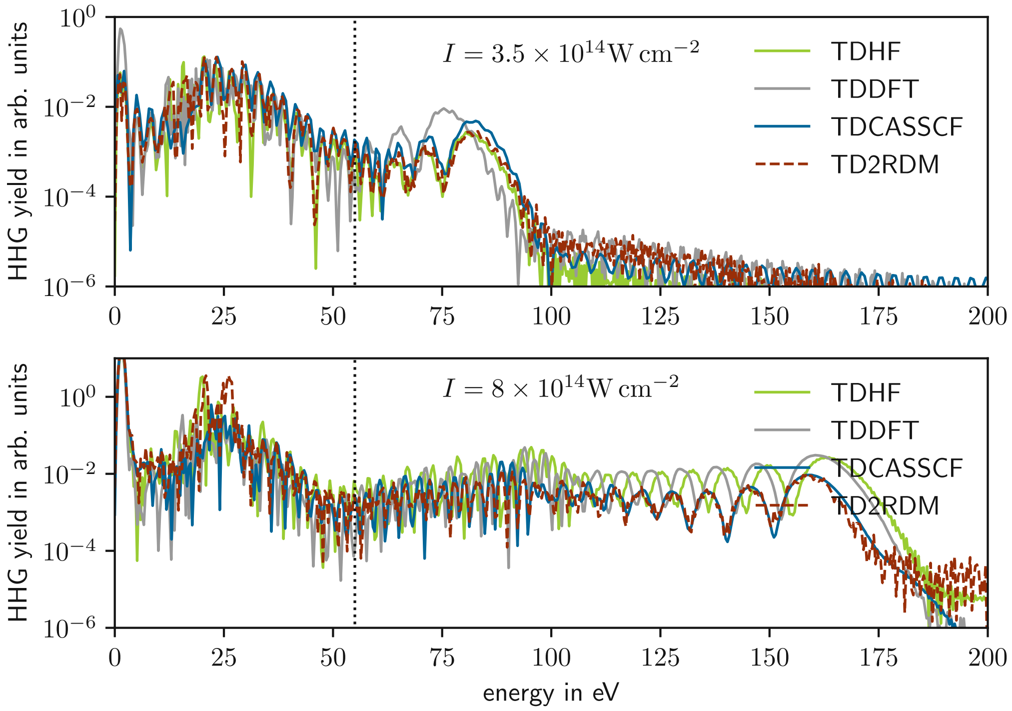

Figure 6.15.: Harmonic yield for HHG in argon driven with a 3 cycle, 780 nm and $I = 3.5 \times 10^{14}$ $\mathrm{W\,cm^{-2}}$ and $I = 8 \times 10^{14}$ $\mathrm{W\,cm^{-2}}$ laser pulse. The results were obtained within TDHF, TDDFT, TDCASSCF and TD2RDM. The cooper minima is marked at 55 eV.

For the higher intensity of the laser field the ionisation probability is about ten times higher than for the lower intensity laser pulse, see Figure 6.16. Two-particle ionisation is for both cases suppressed, with a slight increase after the largest amplitude modulation of the electric field at 1.5 optical cycles.

For the stronger laser pulse of $I = 8 \times 10^{14}$ $\mathrm{W\,cm^{-2}}$ we observe that several natural occupation numbers approach each other, see Figure 6.16, while for the weaker $I = 3.5 \times 10^{14}$ $\mathrm{W\,cm^{-2}}$ pulse they remain practically constant. Overall we end up with a much more mixed systems than we started with for the stronger intensity. The results within TDCASSCF and TD2RDM are similar at the beginning, but at around 3 optical cycles there is an exchange in weight between the outer shell 3p and 3s orbitals within the TD2RDM method that is not reproduced within the TDCASSCF calculations.

When driven with the lower intensity laser field, see upper panel of Figure 6.17, we see only small changes over time in the natural occupation numbers. However, the discrepancies between the occupations from the TDCASSCF and TD2RDM method are relatively large, although being very small on an absolute scale. The discrepancies are very small also for the Frobenius norm of the two-particle cummulant shown in the upper

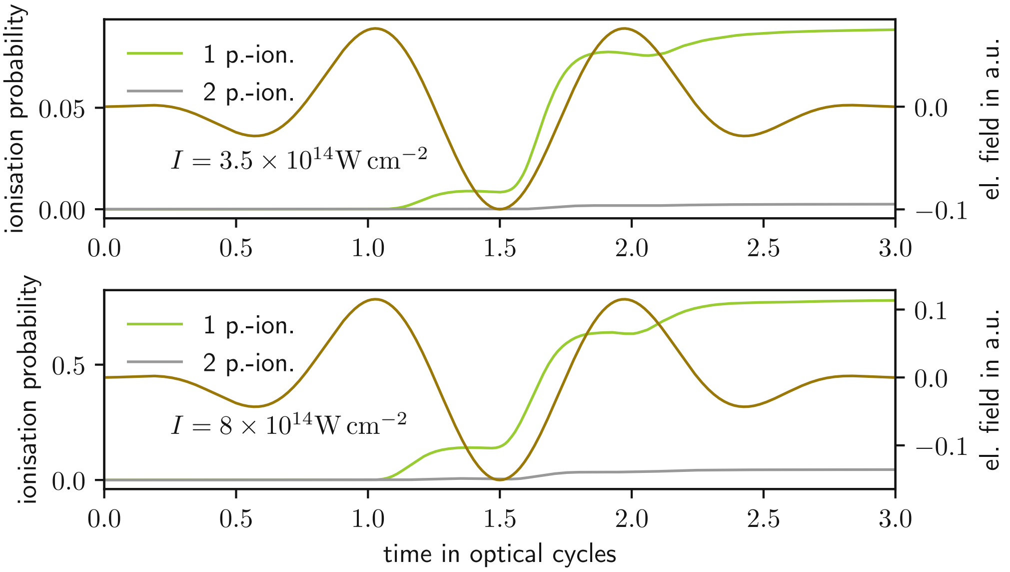

Figure 6.16.: One- and two-particle ionisation probability for argon within the MCTDHF method with a 3 cycles, 780 nm, and $I = 3.5 \times 10^{14}\ \mathrm{W\,cm^{-2}}$ and $I = 8 \times 10^{14}\ \mathrm{W\,cm^{-2}}$ laser pulse.

panel of Figure 6.18. There, similar to the lower intensity case for beryllium discussed in section 6.1, we get an overall reduction in correlations and the TD2RDM method underestimates the correlations. On the contrary, during the $I = 8 \times 10^{14}\ \mathrm{W\,cm^{-2}}$ laser pulse, the change in correlations is large and comparable to the one in Figure 6.4. The discrepancies between the TD2RDM and TDCASSCF methods at the end of the laser field can be explained by the above mentioned spurious coupling between the outer shell 3p and 3s orbitals within the TD2RDM method.

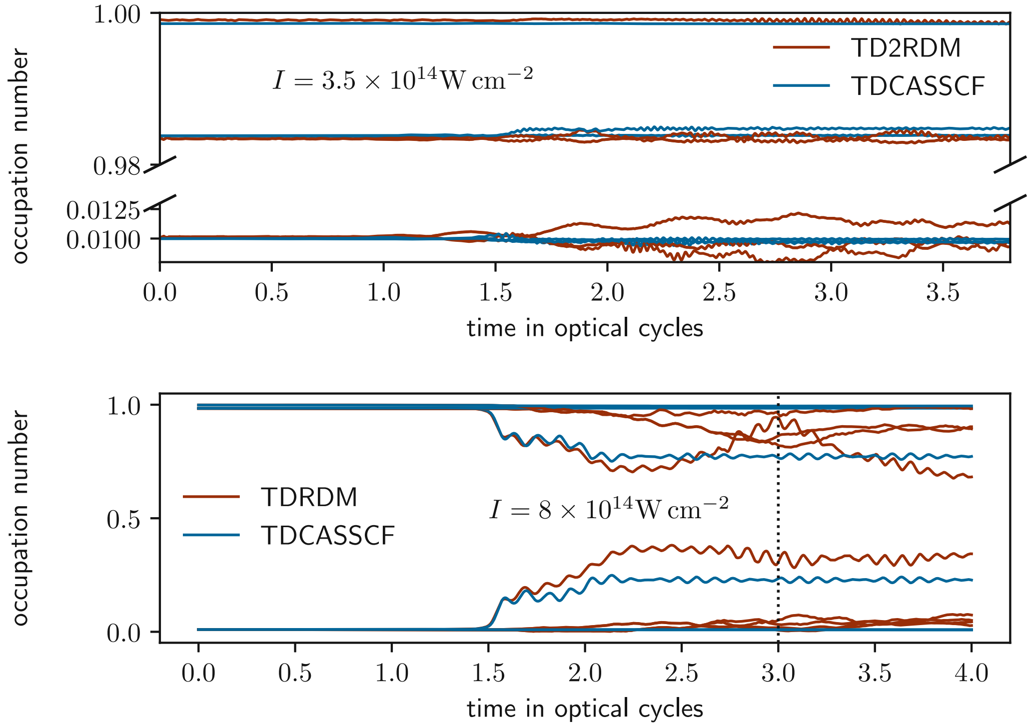

Figure 6.17.: Natural occupation numbers, i.e. eigenvalues of the 1RDM, from the TDCASSCF and TD2RDM calculations in argon with a 3 cycle, 780 nm, $I = 3.5 \times 10^{14}\ \mathrm{W\,cm^{-2}}$ and $I = 8 \times 10^{14}\ \mathrm{W\,cm^{-2}}$ laser pulse.

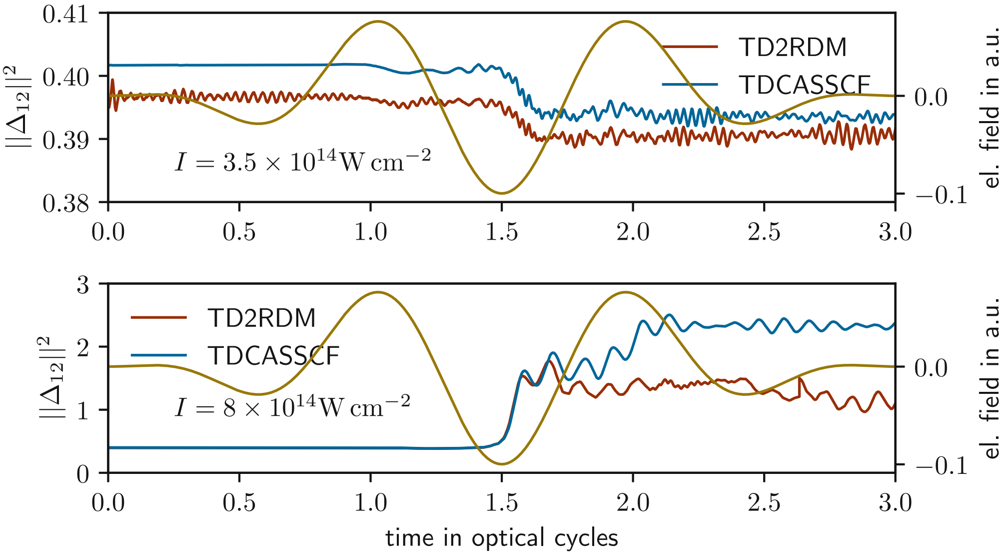

Figure 6.18.: Frobenius norm of the two-particle cummulant for MCTDHF and TD2RDM calculations in argon with a 3 cycles, 780 nm, and $I = 3.5 \times 10^{14}\ \mathrm{W\,cm^{-2}}$ and $I = 8 \times 10^{14}\ \mathrm{W\,cm^{-2}}$ laser pulse.

7. Conclusion and outlook

To sum up, we have applied the TD2RDM method to HHG in large atomic systems such as argon and have demonstrated that the TD2RDM is highly accurate also in this setting. As benchmark methods we have used MCTDHF and TDCASSCF, which make an explicit ansatz for the multi-electron wavefunction and thus scale exponentially with particle number. TD2RDM in contrast scales only linearly. Furthermore, we have demonstrated that the TD2RDM formalism allows for the same reduction of dimensionality as TDCASSCF by applying the concept of active and core orbitals. Base on our multi-electron calculations, we have quantified the role of electron correlations using correlation measures from quantum information theory.
For this investigation of correlations, we have analysed the time behaviour of different correlation measures for systems of indistinguishable fermions. Thereby, the Frobenius norm of the two-particle cummulant has shown the largest dynamical range, while also being the most natural measure for our method. However, we have observed that all measures show essentially the same time dependence. Moreover, correlation measures such as the entropy of reduced density matrices of the 1RDM and 2RDM become indistinguishable when rescaled by their initial value. They carry thus the same information on the dynamical process.
Based on these correlation measures we found two different regimes during HHG. A regime where correlations increase due to the strong laser field to values larger than the initial correlations in the system ,and a regime, where the change of correlations is comparable or smaller than the initial correlations in the system. In the second regime, the overall ionisation probability is small and of the order of 10%. In this regime using a time-frequency analysis where have found several structures in the HHG yield as well as in our two-particle correlation measures that indicate the presence of correlated two-particle dynamics such as two-particle resonances. these results are so far preliminary and we leave it for future studies to quantify the observed effects in more detail.

Moreover, we want to extend our studies to even larger atoms, such as xenon, for which we already presented some preliminary results. There, especially the giant dipole resonance is interesting as an example of a prominent electron correlation effect.

Acknowledgements

I would like to thank my advisor Iva Březinová for her time and patience in explaining things and answering all my physics questions. The discussions with her and the rest of the group, Elias Pescoller and Markus Stimpfle, rekindled my passion for physics.
I would like to thank Fabian Lackner, for the TD2RDM code and for always finding time to help me troubleshooting. Furthermore, I would like to thank Kenichi Ishikawa and Takeshi Sato for the MCTDHF code. I would like to thank all the nice people at the institute who made me feel welcome and I shared chocolate with in the breaks.
I would like to thank my family for supporting me throughout my studies both financially and mentally. Especially my mother, with her understanding manner. I would like to thank my friends I made during my studies, for sharing this experiences and problems along the way. Finally I would like to thank Florian Schnabel for his love and patience.

A. Input parameters for numerical results

In the following, we quantify the values of input parameter as required by the current code. This is meant to serve as reference for follow up calculations using the code and to guarantee reproduce-ability of our numerical results.

For all calculations the thresholds for the propagator are set to
$h1rat\_maxcyc = 40$,
$h1rat\_thresh = 1.0E-13$,
$h1itr\_maxcyc = 40$, and
$h1itr\_thresh = 1.0E-12$, and
$etd\_cisplit = -1$.
The expansions in l quantum numbers are terminated at
$lmax1 = 47$ Equation 3.17 and
$lmax2 = 47$ Equation 3.16, furthermore
$jfc\_implicit = true$ and
$xfc\_implicit = true$ are set.

In order to perform TD2RDM calculations instead of MCTDHF within the code
$disable\_cic = true$ is set. The reconstruction is for all TD2RDM calculations set to
$reconstruction\_type = NY + CC$ and the purification
$purification\_type = reduce$,
$purification\_step = 40$, and
$purification\_error = 0$.

For the TDDFT calculations the exchange-correlation functional is chosen by $dft\_type = 131$.

The averaging calculations for chapter 5 all use the same propagator $prop\_type = split2$ where the gauge choice is set to $\langle\phi_i| i\partial_t |\phi_j\rangle = 0$ with the parameters $oorot\_type = 0$ and $split\_type = 0$. Furthermore, the orbitals are kept fixed with $fixorb = true$. For beryllium the averaging time of 30 a.u. is set via $average\_2rdm = 30$, neon and argon use an averaging time of 50 a.u.. The grids are set the same, as for the ground-state calculations, i.e.

$nfe = 20$
$grid:$
0.0 40 20 20

for beryllium and neon and

$nfe = 16$
$grid:$
0.0 2.0 20 2
2.0 30 20 14

for argon.

The time-propagations shown in chapter 5 all use the same parameters as the corresponding calculations in chapter 6. All time propagations use the same propagator $prop\_type = etdrb$ and the gauge choice $\langle \phi_i | i\partial_t \left|\phi_j\right\rangle = h^i_j$ is set via
$oorot\_type = 0$ and
$split\_type = 1$.
For the laser field we use the velocity gauge
$gauge = velocity2$ and
$num\_field = 1$,
$delay = 0.0$,
$cep = 90.0$, and
$env\_type = sin2$ are set.

For the beryllium calculations in section 6.1 with $I = 4 \times 10^{14}\ \mathrm{W\,cm^{-2}}$, $fint = 4.0e14$, and $\lambda = 800$ nm, $wlen = 800$, and two cycles, $numcyc = 2$, are set. We propagate for $cyctot = 3$ with $nstep = 20000$ per cycle, on a grid of

$nfe = 50$
$grid:$
0.0 200 20 50

The same parameters are also used for the neon calculation, except $fint = 1.0e15$. For the beryllium calculations with the lower field intensity of $fint = 5.0e13$, and $wlen = 2000$ a larger grid of

$nfe = 75$
$grid:$
0.0 300 20 75

is used. For the argon calculations $wlen = 780$, $numcyc = 3$, $cyctot = 4$, and $nstep = 40000$ are set. For the $fint = 3.5e14$ calculations a grid of

$nfe = 61$
$grid :$
0.0 2.0 20 2
2.0 120 20 59

is used. While for $fint = 8.0e14$,

$nfe = 101$
$grid :$
0.0 2.0 20 2
2.0 200 20 99

is used.

B. Preliminary xenon results

Here we present preliminar results of xenon calculations. Figure B.1 shows the HHG spectrum of xenon for a two cycle, 300 nm, and $I = 5 \times 10^{15}$ $\mathrm{W\,cm^{-2}}$ obtained with TDHF and TD2RDM. The region, where the giant-dipole resonance is expected, is marked. It is quite striking that both methods give very similar results. The reason could be the fact, that the laser parameters lead to very weak ionisation probabilities. However, presently we cannot exclude a numerical issue. Nonetheless, correlated xenon calculations for HHG are in the scope of the TD2RDM method.

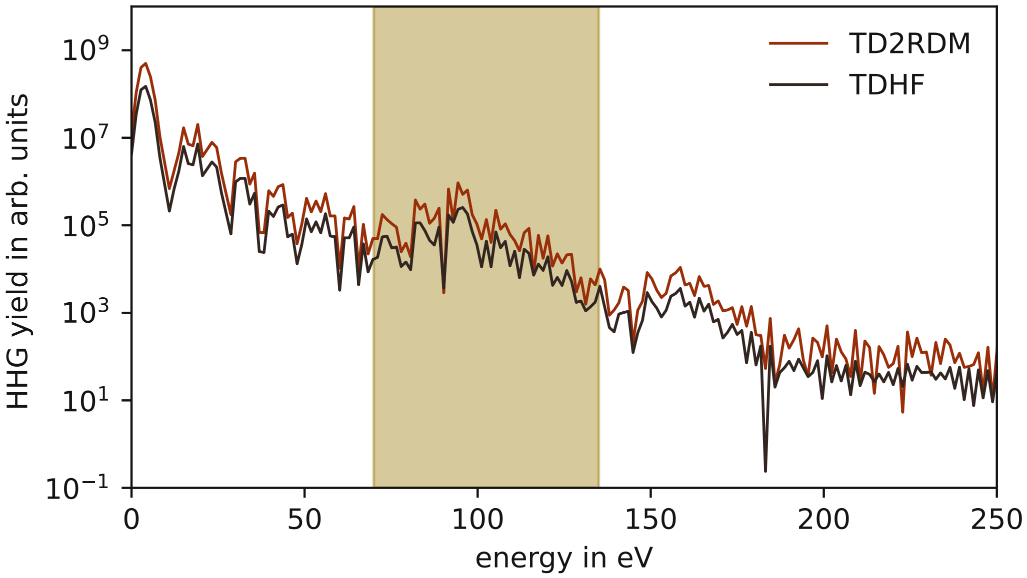

Figure B.1.: HHG spectrum for xenon from TDHF and TD2RDM calculations with a 2 cycle laser pulse with 300 nm and $I = 5 \times 10^{15}$. The highlighted area shows the spectral regime of the giant dipole resonance.

Bibliography

[1] A. McPherson, G. Gibson, H. Jara, U. Johann, T. S. Luk, I. A. McIntyre, K. Boyer, and C. K. Rhodes. *Studies of multiphoton production of vacuum-ultraviolet radiation in the rare gases*. J. Opt. Soc. Am. B **4**, 595 (1987).

[2] M. Ferray, A. L'Huillier, X. F. Li, L. A. Lompre, G. Mainfray, and C. Manus. *Multiple-harmonic conversion of 1064 nm radiation in rare gases*. J. Phys. B: At. Mol. Opt. Phys. **21**, L31 (1988).

[3] T. Popmintchev, M.-C. Chen, D. Popmintchev, P. Arpin, S. Brown, S. Ališauskas, G. Andriukaitis, T. Balčiunas, O. D. Mücke, A. Pugzlys, A. Baltuška, B. Shim, S. E. Schrauth, A. Gaeta, C. Hernández-García, L. Plaja, A. Becker, A. Jaron-Becker, M. M. Murnane, and H. C. Kapteyn. *Bright Coherent Ultrahigh Harmonics in the keV X-ray Regime from Mid-Infrared Femtosecond Lasers*. Science **336**, 1287 (2012).

[4] R. Borrego-Varillas, M. Lucchini, and M. Nisoli. *Attosecond spectroscopy for the investigation of ultrafast dynamics in atomic, molecular and solid-state physics*. Rep. Prog. Phys. **85**, 066401 (2022).

[5] M. Schultze, M. Fieß, N. Karpowicz, J. Gagnon, M. Korbman, M. Hofstetter, S. Neppl, A. L. Cavalieri, Y. Komninos, T. Mercouris, C. A. Nicolaides, R. Pazourek, S. Nagele, J. Feist, J. Burgdörfer, A. M. Azzeer, R. Ernstorfer, R. Kienberger, U. Kleineberg, E. Goulielmakis, F. Krausz, and V. S. Yakovlev. *Delay in Photoemission*. Science **328**, 1658 (2010).

[6] M. Isinger, R. J. Squibb, D. Busto, S. Zhong, A. Harth, D. Kroon, S. Nandi, C. L. Arnold, M. Miranda, J. M. Dahlström, E. Lindroth, R. Feifel, M. Gisselbrecht, and A. L'Huillier. *Photoionization in the time and frequency domain*. Science **358**, 893 (2017).

[7] C. Spielmann, N. H. Burnett, S. Sartania, R. Koppitsch, M. Schnürer, C. Kan, M. Lenzner, P. Wobrauschek, and F. Krausz. *Generation of Coherent X-rays in the Water Window Using 5-Femtosecond Laser Pulses*. Science **278**, 661 (1997).

[8] J. M. Schins, P. Breger, P. Agostini, R. C. Constantinescu, H. G. Muller, G. Grillon, A. Antonetti, and A. Mysyrowicz. *Observation of Laser-Assisted Auger Decay in Argon*. Phys. Rev. Lett. **73**, 2180 (1994).

[9] P. M. Paul, E. S. Toma, P. Breger, G. Mullot, F. Augé, P. Balcou, H. G. Muller, and P. Agostini. *Observation of a Train of Attosecond Pulses from High Harmonic Generation*. Science **292**, 1689 (2001). Publisher: American Association for the Advancement of Science.

[10] M. Hentschel, R. Kienberger, C. Spielmann, G. A. Reider, N. Milosevic, T. Brabec, P. Corkum, U. Heinzmann, M. Drescher, and F. Krausz. *Attosecond metrology*. Nature **414**, 509 (2001).

[11] A. L'Huillier, K. J. Schafer, and K. C. Kulander. *Theoretical aspects of intense field harmonic generation*. J. Phys. B: At. Mol. Opt. Phys. **24**, 3315 (1991).

[12] J. L. Krause, K. J. Schafer, and K. C. Kulander. *High-order harmonic generation from atoms and ions in the high intensity regime*. Phys. Rev. Lett. **68**, 3535 (1992).

[13] P. B. Corkum. *Plasma perspective on strong field multiphoton ionization*. Phys. Rev. Lett. **71**, 1994 (1993).

[14] M. Lewenstein, P. Balcou, M. Y. Ivanov, A. L'Huillier, and P. B. Corkum. *Theory of high-harmonic generation by low-frequency laser fields*. Phys. Rev. A **49**, 2117 (1994).

[15] T. Sato and K. L. Ishikawa. *Time-dependent complete-active-space self-consistent-field method for multielectron dynamics in intense laser fields*. Physical Review A **88**, 023402 (2013).

[16] T. Sato and K. L. Ishikawa. *Time-dependent complete-active-space self-consistent-field method for multielectron dynamics in intense laser fields*. Physical Review A **88**, 023402 (2013).

[17] D. Hochstuhl and M. Bonitz. *Time-dependent restricted-active-space configuration-interaction method for the photoionization of many-electron atoms*. Phys. Rev. A **86**, 053424 (2012).

[18] S. Pabst and R. Santra. *Strong-Field Many-Body Physics and the Giant Enhancement in the High-Harmonic Spectrum of Xenon*. Physical Review Letters **111**, 233005 (2013).

[19] F. Lackner, I. Březinová, T. Sato, K. L. Ishikawa, and J. Burgdörfer. *High-harmonic spectra from time-dependent two-particle reduced-density-matrix theory*. Physical Review A **95**, 033414 (2017).

[20] T. Sato, K. L. Ishikawa, I. Březinová, F. Lackner, S. Nagele, and J. Burgdörfer. *Time-dependent complete-active-space self-consistent-field method for atoms: Application to high-order harmonic generation*. Physical Review A **94**, 023405 (2016).

[21] L. Ding and C. Schilling. *Correlation paradox of the dissociation limit: A quantum information perspective*. J. Chem. Theory Comput. **16**, 4159 (2020). ArXiv:2001.04858 [quant-ph].

[22] R. Weissenbilder, S. Carlström, L. Rego, C. Guo, C. M. Heyl, P. Smorenburg, E. Constant, C. L. Arnold, and A. L'Huillier. *How to optimize high-order harmonic generation in gases*. Nat Rev Phys **4**, 713 (2022).

[23] L. V. Keldysh. *Ionization in the field of a strong electromagnetic wave*. In *Selected Papers of Leonid V Keldysh*, pp. 56–63. WORLD SCIENTIFIC (2023).

[24] Z. Chang. *Fundamentals of attosecond optics*. CRC Press, Boca Raton (2011).

[25] M. V. Ammosov and V. P. Krainov. *Tunnel ionization of complex atoms and of atomic ions in an alternating electromagnetic field*. Sov. Phys. JETP 64, 1191 (1986) .

[26] A. Kramida, Yu. Ralchenko, J. Reader, and and NIST ASD Team. NIST Atomic Spectra Database (ver. 5.10), [Online]. Available: `https://physics.nist.gov/asd` [2023, April 17]. National Institute of Standards and Technology, Gaithersburg, MD. (2022).

[27] X.-M. Tong and S.-I. Chu. *Theoretical study of multiple high-order harmonic generation by intense ultrashort pulsed laser fields: A new generalized pseudospectral time-dependent method*. Chemical Physics **217**, 119 (1997).

[28] J. Feist, S. Nagele, R. Pazourek, E. Persson, B. I. Schneider, L. A. Collins, and J. Burgdörfer. *Nonsequential two-photon double ionization of helium*. Phys. Rev. A **77**, 043420 (2008).

[29] J. M. Ngoko Djiokap and A. F. Starace. *Evidence of the $2s2p(^1P)$ doubly excited state in the harmonic generation spectrum of helium*. Phys. Rev. A **84**, 013404 (2011).

[30] N. Rohringer, A. Gordon, and R. Santra. *Configuration-interaction-based time-dependent orbital approach for ab initio treatment of electronic dynamics in a strong optical laser field*. Phys. Rev. A **74**, 043420 (2006).

[31] F. Lackner. *Time-dependent two-particle reduced density matrix theory: application to multi-electron atoms and molecules in strong laser pulses*. Wien (2017).

[32] W. Auzinger, I. Březinová, A. Grosz, H. Hofstätter, O. Koch, and T. Sato. *Efficient adaptive exponential time integrators for nonlinear Schrödinger equations with nonlocal potential*. Journal of Computational Mathematics and Data Science **1**, 100014 (2021).

[33] M. A. L. Marques, M. J. T. Oliveira, and T. Burnus. *Libxc: A library of exchange and correlation functionals for density functional theory*. Computer Physics Communications **183**, 2272 (2012).

[34] C. A. Ullrich. *Time-dependent density-functional theory: concepts and applications*. Oxford graduate texts. Oxford University Press, Oxford New York, reprinted, with corrections edition (2016).

[35] M. Piris and P. Otto. *One-particle density matrix functional for correlation in molecular systems*. International Journal of Quantum Chemistry **94**, 317 (2003). _eprint: https://onlinelibrary.wiley.com/doi/pdf/10.1002/qua.10707.

[36] R. G. Parr and W. Yang. *Density-functional theory of atoms and molecules*. Number 16 in International series of monographs on chemistry. Oxford Univ. Press [u.a.], New York, NY, 1. iss. as ... paperback edition (1994).

[37] F. Lackner, I. Březinová, T. Sato, K. L. Ishikawa, and J. Burgdörfer. *Propagating two-particle reduced density matrices without wave functions*. Physical Review A **91**, 023412 (2015).

[38] D. A. Mazziotti. *Complete reconstruction of reduced density matrices*. Chemical Physics Letters **326**, 212 (2000).

[39] K. Yasuda and H. Nakatsuji. *Direct determination of the quantum-mechanical density matrix using the density equation. II*. Phys. Rev. A **56**, 2648 (1997).

[40] D. A. Mazziotti. *Structure of Fermionic Density Matrices: Complete N-Representability Conditions*. Phys. Rev. Lett. **108**, 263002 (2012).

[41] J.-P. Joost, N. Schlünzen, H. Ohldag, M. Bonitz, F. Lackner, and I. Březinová. *Dynamically screened ladder approximation: Simultaneous treatment of strong electronic correlations and dynamical screening out of equilibrium*. Phys. Rev. B **105**, 165155 (2022).

[42] R. Horodecki, P. Horodecki, M. Horodecki, and K. Horodecki. *Quantum entanglement*. Rev. Mod. Phys. **81**, 865 (2009).

[43] S. Donsa, F. Lackner, J. Burgdörfer, M. Bonitz, B. Kloss, A. Rubio, and I. Březinová. *Non-equilibrium correlation dynamics in the one-dimensional Fermi-Hubbard model: A testbed for the two-particle reduced density matrix theory* (2023). ArXiv:2303.04576 [cond-mat].

[44] J. T. Skolnik and D. A. Mazziotti. *Cumulant reduced density matrices as measures of statistical dependence and entanglement between electronic quantum domains with application to photosynthetic light harvesting*. Phys. Rev. A **88**, 032517 (2013).

[45] H. J. Wörner, H. Niikura, J. B. Bertrand, P. B. Corkum, and D. M. Villeneuve. *Observation of Electronic Structure Minima in High-Harmonic Generation*. Phys. Rev. Lett. **102**, 103901 (2009).

[46] J. D. Hunter. *Matplotlib: A 2D graphics environment*. Computing in Science & Engineering **9**, 90 (2007).

[47] Y. Li, T. Sato, and K. L. Ishikawa. *High-order harmonic generation enhanced by laser-induced electron recollision*. Phys. Rev. A **99**, 043401 (2019).

[48] J. W. Cooper. *Photoionization from Outer Atomic Subshells. A Model Study*. Phys. Rev. **128**, 681 (1962).